

**Probabilistic Printability Maps for Laser Powder Bed Fusion via Functional Calibration
and Uncertainty Propagation**

A Technical Report submitted to the Department of Materials Science and Engineering


Presented to the Faculty of the School of Engineering and Applied Science
University of Virginia • Charlottesville, Virginia

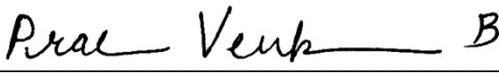
In Partial Fulfillment of the Requirements for the Degree
Bachelor of Science, School of Engineering

Nicholas Wu

Spring, 2023

On my honor as a University Student, I have neither given nor received unauthorized aid on this assignment as defined by the Honor Guidelines for Thesis-Related Assignments.

Signature  Date 04/27/2023
Nicholas Wu

Approved  B Date 04/27/2023
Prasanna V. Balachandran, Department of Materials Science and Engineering

Probabilistic Printability Maps for Laser Powder Bed Fusion via Functional Calibration and Uncertainty Propagation

Nicholas Wu

Department of Materials Science and Engineering
University of Virginia
Charlottesville, VA 22904

Brendan Whalen

Department of Mechanical and Aerospace Engineering
University of Virginia
Charlottesville, VA, 22904

Ji Ma

Department of Materials Science and Engineering
University of Virginia
Charlottesville, VA 22904

Prasanna V. Balachandran*

Department of Materials Science and Engineering
Department of Mechanical and Aerospace Engineering
University of Virginia
Charlottesville, VA 22904

In this work, we develop an efficient computational framework for process space exploration in laser powder bed fusion (LPBF) based additive manufacturing technology. This framework aims to find suitable processing conditions by characterizing the probability of encountering common build defects. We employ a Bayesian approach towards inferring a functional relationship between LPBF processing conditions and the unobserved parameters of laser energy absorption and powder bed porosity. The relationship between processing conditions and inferred laser energy absorption is found to have good correspondence to literature measurements of powder bed energy absorption using calorimetric methods. The Bayesian approach naturally enables uncertainty quantification and we demonstrate its utility by performing efficient forward propagation of uncertainties through the modified Eagar-Tsai model to obtain estimates of melt pool geometries, which we validate using out-of-sample experimental data from the literature. These melt pool predictions are then used to compute the probability of occurrence of keyhole and lack-of-fusion based defects using geometry-based crite-

ria. This information is summarized in a probabilistic printability map. We find that the probabilistic printability map can describe the keyhole and lack of fusion behavior in experimental data used for calibration, and is capable of generalizing to wider regions of processing space. This analysis is conducted for SS316L, IN718, IN625, and Ti6Al4V using melt pool measurement data retrieved from the literature.

1 Introduction

Additive manufacturing (AM) technologies are a class of manufacturing methods in which products are built by depositing and fusing raw material in successive passes and layers. In particular, metal-based AM technologies like Laser Powder Bed Fusion (LPBF) successively fuse layers of metal powder using a scanning laser [1]. There has been an increased interest in the technology recently due to the potential advantages that AM offers over traditional techniques, such as the ability to enable on-demand manufacturing and greater design flexibility. A major challenge is controlling and understanding variability from print-to-print

*Address all correspondence to this author. Email: pvb5e@virginia.edu

and machine-to-machine [2].

A variety of modeling approaches have been used to study the LPBF process and establish the relationship between processing parameters and defects. A common approach is to focus on modeling the melt pool geometry. This is due to the strong correlation between the melt pool geometry and common defects encountered in LPBF. Tang et al. [3] used melt pool data to accurately predict porosity arising from insufficient overlap of the melt pool (lack-of-fusion). Cunningham et al. [4] studied pore formation in Ti6Al4V samples and observed that excess power density caused keyholing pores. Scime and Beuth [5] performed ex-situ characterization of IN718 single tracks and established the relationship between melt pool geometries and porosity defects arising from keyholing, lack-of-fusion, and balling.

Approaches for modeling the melt pool range from high-resolution multi-physics simulations of the LPBF process (e.g [6]) to simpler analytical models, e.g the Eagar-Tsai (ET) model [7] or the Rosenthal model [8]. Although high-fidelity simulations and finite-element methods can more accurately reflect the complex physical phenomena in the LPBF process, they are more computationally expensive, making them unsuitable for usage in studies that aim to characterize a large number of experimental conditions. Alternatively, one can choose to employ a lower-fidelity, computationally cheap analytical model. Although these models display some inconsistency with experimental measurements, they are able to capture the essential relationship between processing parameters and melt pool geometries, and have successfully been used in guiding parameter exploration and mapping process space [9, 10].

Data-driven and machine learning (ML) modeling approaches also have gained maturity, and can be used in tandem with simulation modeling and experimental data to extract knowledge about the LPBF process. The review by Qin et al. [11] details applications of ML in AM, which can include in-situ process monitoring and using data mining to investigate correlations between processing parameters, materials properties, and melt pool geometry. However, purely ML approaches require large amounts of data and can have a black-box nature. Instead, one can combine ML approaches with simulation models. One such method is via a calibration routine, which fits the model to experimental data by finding a suitable value for an unobserved parameter of the model. For more expensive models, often ML surrogates are used in calibration. This involves approximation by a fast-running ML model, e.g Gaussian process regression [12–14]. This approximation is not necessary for cheaper models.

A critical parameter that is difficult to measure in real time during the manufacturing process is the laser energy absorption, as it is closely linked to physical phenomena governing the transition between conduction mode welding and keyhole mode welding. Thus, absorptivity is commonly selected as a calibration parameter in modeling studies of LPBF [15–17]. It is typical to approximate a material's laser absorptivity with a value which is constant over the entire processing space. This is a reasonable approximation for conduction-mode welding, but breaks down in the keyhole

regime as the keyhole shape and vapor depression below the laser influences the absorption of laser energy [18]. Experimental studies have demonstrated the dependence of laser energy absorption on processing parameters [19, 20].

Due to the nature of LPBF as a variable process, there has been interest and developments in applying techniques from the field of uncertainty quantification (UQ) to modeling techniques in LPBF [21]. Uncertainty in modeling may arise due to inherent randomness in the underlying physical processes (aleatoric uncertainty), or due to unknown parameters of the physical system (epistemic uncertainty). A natural way to model uncertainty in parameters in calibration studies is to employ a Bayesian approach towards inferring unobserved parameters [17, 22, 23]. Rather than providing a point estimate, Bayesian methods combine prior knowledge with experimental data to provide uncertain estimates of unobserved parameters [24]. After carrying out inference, one is given uncertain estimates for unobserved parameters, which cannot be compared directly to experimental data. Then, it is necessary to use uncertainty propagation to obtain useful estimates for comparison. An efficient approach towards uncertainty propagation that has been explored in the AM literature is the polynomial chaos method [25], which requires significantly less model evaluations than standard Monte-Carlo approaches to achieve comparable estimation quality.

Once a model has been fit, additional work must be done to extract insights about the parameter space. A printability map uses the model to summarize the relationship between processing parameters and likely defects in a single graphic. Typically, regions of the laser power/laser scan speed space are labeled according to the likely defect; e.g keyhole, lack of fusion, or balling [26, 27]. These labels may be based upon scaling ratios of the melt pool [10]. Previous studies investigating frameworks for constructing printability maps have mostly employed deterministic models, resulting in sharp well-defined transition boundaries between melting regimes. However, it may not be realistic to treat the boundaries predicted by a model to be so well-defined, due to the uncertainties in the modeling process and in the LPBF process itself. A principled approach is to propagate modeling uncertainties into the printability map itself. Vela et al. [28] created probabilistic maps exploring the effect of alloy composition on balling. Wang et al. investigated the propagation of uncertainty into predictions of final part porosity [22]. Ye et al. [29] explored probabilistic maps for Directed Energy Deposition, but as of yet this has not been explored for the case of melt pools in LPBF.

In this work, we employ a modified version of the ET model to develop an efficient computational framework with UQ for exploration of the LPBF process space. First, in contrast to previous calibration studies using the ET model, we infer laser-power and laser-speed dependent values for the calibration parameters in our study. This dependence better reflects the underlying physical processes involved in LPBF, and the inference procedure allows for flexibility in modeling results across different experiments and conditions. Second, we utilize an efficient uncertainty propagation routine based upon polynomial chaos to propagate uncertainties aris-

ing from parameter estimation through the ET model. Finally, the uncertainty propagation routine is used to construct a new variant of the printability map taking these uncertainties into account (the *probabilistic* printability map). This approach will provide a comprehensive approach in characterizing the printability of materials and assisting in process optimization. The workflow of our approach is visualized in Figure 1.

2 Methods

2.1 Modified Eagar-Tsai model and thermophysical properties of materials

The modified ET model used in this work was first developed by Whalen et al [23], which adapts the original ET model by the inclusion of parameters specific to LPBF. In particular, these are apparent absorptivity and porosity parameters. For a full description of the model, we refer back to the original work [23], but provide a brief overview of the parameters of interest here.

The original ET model [7] may be used to predict the temperature field arising from a Gaussian heat source moving over a flat metal plate. The heat source is described by the parameters of speed v , power P , and the distribution parameter of the heat source σ , i.e the standard deviation of the Gaussian beam. The substrate is described by the thermal diffusivity a , the initial temperature T_0 , the critical (melting) temperature T_c , and the density ρ . Given these parameters, the model outputs an approximation of the temperature field under the laser. From this, we obtain an estimate of the melt pool dimensions by selecting isotherms at the melting temperature of the material.

In the modified ET model, we incorporate the parameters of apparent laser absorptivity (η) and apparent powder bed porosity (ϕ). Temperature-dependent thermophysical properties were retrieved from the literature, and are enumerated for each material in Table 1. Apparent absorptivity is a coefficient on the power input, i.e

$$P_{\text{eff}} = \eta P$$

Thus, an absorptivity of $\eta = 1$ corresponds to full laser absorption. Porosity is inversely related to the powder bed packing fraction. This quantity enters the model as an effective density and an effective thermal conductivity.

$$\rho_{\text{eff}} = (1 - \phi)\rho_{\text{solid}}$$

Thus, a value of ϕ near 1 indicates a very low packing density, and a value near 0 indicates a very high (near solid) packing density. The effective thermal conductivity is computed as

$$\kappa_{\text{eff}} = \kappa_{\text{solid}} \frac{1 + (k_e - 1)B\phi}{1 - B\psi\phi}$$

by the Lewis-Nielson model [30], where k_e is the Einstein coefficient. B is a constant capturing the relationship between the thermal conductivity of the material and the thermal conductivity of the inert gas. ψ depends on the maximum attainable powder bed porosity and the current porosity ϕ [23, 30]. We selected argon as the inert gas, and its temperature-dependent thermal conductivity was retrieved from [31] and [32].

In LPBF, it is known that powder bed conditions can be complex and heterogeneous across different locations in the powder bed, and so a single scalar such as the apparent powder bed porosity ϕ is unlikely to realistically describe these conditions. However, as changes in apparent powder porosity can influence the thermal conductivity, appropriate calibration of the apparent porosity parameter has the possibility of capturing LPBF phenomena that influence heat transfer and energy absorption within the melt pool, which are not explicitly modeled by the ET model. These may include Marangoni convection and vapor depression formation, which affect the melt pool width and melt pool depth respectively. In this sense, including apparent absorptivity along with apparent porosity gives the ET Model additional flexibility in modeling thermal phenomena that are influential in melt pool formation in LPBF while retaining a high degree of computational efficiency. Previous studies have examined the utility of including such parameters within the modeling process [15, 33].

Material	References
IN625	[34] [35] [36]
IN718	[37] [38] [39] [40]
SS316L	[41] [42]
Ti6Al4V	[43]

Table 1. Sources for thermophysical properties of the studied materials.

2.2 Bayesian calibration of absorptivity and porosity

Although the modified ET model incorporates additional information that the original ET model does not, it requires the use of a parameter calibration procedure to improve agreement with experiment. We opt to use the Bayesian calibration procedure. A key reference for the Bayesian calibration of computer models is Kennedy and O’Hagan [44]. We adapt their inference paradigm for the ET model to balance ease of modeling, computational efficiency, and predictive accuracy given the underlying physical phenomena in LPBF.

Given an experimental dataset, Bayesian calibration of a computer model requires the specification of at least 3 elements: (1) the *model* to be calibrated; in this case the ET model. (2) A *likelihood function*, specifying the likelihood of unobserved parameters given the experimental data and

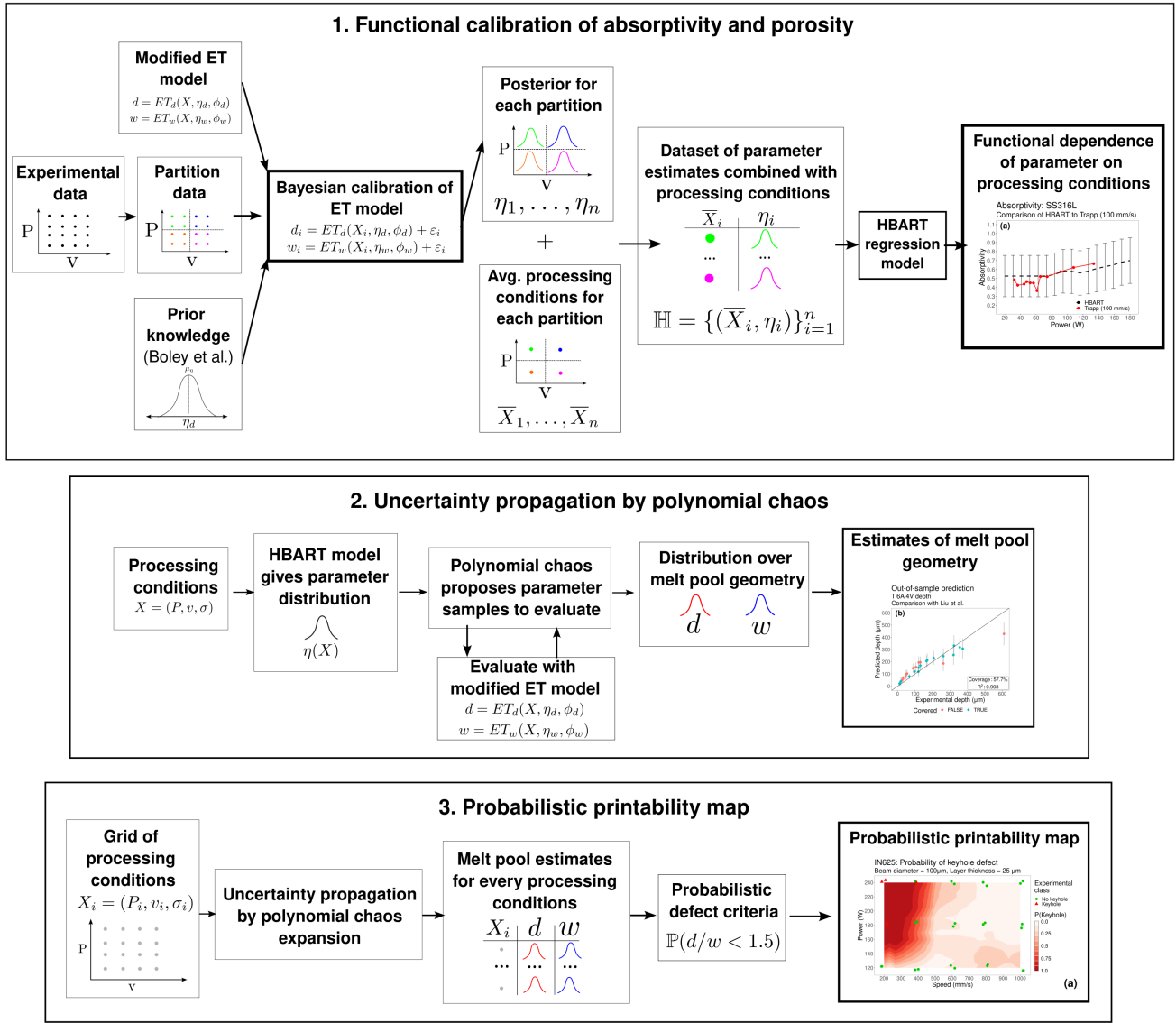


Fig. 1. The workflow of our computational modeling approach. Functional calibration of absorptivity and porosity is discussed in Sections 2.1-2.3. In this step, we first utilized Bayesian inference to calibrate the modified ET numerical model [23] by inferring values for laser energy absorption and powder bed porosity based on limited experimental data from the literature. Then, we built two sets of independent data-driven models using the non-linear heteroscedastic Bayesian additive regression trees (HBART) method that links the LPBF processing conditions with the parameters of (1) absorption and (2) powder bed porosity. These HBART models allow us to predict, along with the associated uncertainties, the absorptivity and powder bed porosity for the entire LPBF processing space. In the uncertainty propagation step (discussed in Section 2.4), we combined predictions from HBART with polynomial chaos expansion and the modified ET model to predict the melt pool geometries (depth and width), along with the associated uncertainties. The final outcome of our approach is a probabilistic printmap (discussed in Section 2.5) that uses the predictions from the previous steps to delineate regions in the processing space in terms of the probability of occurrence of build defects, namely keyhole and lack of fusion. In the previous work, Whalen et al. developed the Bayesian inference approach for calibrating the modified ET model using experimental data of 316L stainless steel and constructed deterministic printability maps [23]. In this work, we have expanded the methodology by formally modeling uncertainty at each stage of the process. We use HBART to model an uncertain parameter response surface, and employ state-of-the-art uncertainty propagation techniques such as polynomial chaos expansions to rigorously construct probabilistic printability maps. We demonstrate the promise of this approach on a number of important engineering alloys, namely SS316L, IN625, IN718 and Ti6Al4V.

the model. (3) *Prior distributions*, which can be used encode expert knowledge about likely parameter values prior to fitting to data. A notable feature of Bayesian inference is that it outputs a probability distribution for an unknown param-

eter rather than a point estimate. This distribution is known as a *posterior distribution* [24], and this feature is particularly desirable for uncertainty analysis. A standard procedure for computing the posterior is Markov Chain Monte Carlo

(MCMC) [45].

Let $ET_d(X, \phi, \eta)$ and $ET_w(X, \phi, \eta)$ be the functions which respectively return the melt pool depth and width as computed by the modified ET Model. X is a vector of processing conditions $X = [P, V, \sigma]$ where P is laser power, V is laser speed, and σ is the distribution parameter of the laser beam. ϕ and η again denote the powder porosity and absorptivity respectively. Let $\mathbb{D} = \{(X_i, d_i, w_i)\}_{i=1}^n$ denote the experimental melt pool measurement data. $X_i = [P_i, V_i, \sigma_i]$ is the set of processing parameters associated with the i th measurement, and d_i, w_i denote the measured depth and width.

We infer the unobserved parameters of porosity ϕ and absorptivity η , and estimate separate sets of parameters for the depth and the width, resulting in four estimates: ϕ_d and η_d for the depth, and ϕ_w and η_w for the width. Following the notation of Kennedy and O’Hagan [44], this is written as:

$$\begin{aligned} w_i &= ET_w(X_i, \phi_w, \eta_w) + \varepsilon_i \\ d_i &= ET_d(X_i, \phi_d, \eta_d) + \varepsilon_i \end{aligned}$$

where the noise is assumed to be Gaussian with $\varepsilon_i \sim \mathcal{N}(0, \sigma_\varepsilon^2)$. We set the standard deviation of the noise as $\sigma_\varepsilon = 15$ in both inference schemes.

While depth and width are unlikely to have the same variation experimentally, without further information prior to acquiring calibration data, this is a reasonable simplifying assumption that reduces the computational burden. Furthermore, variation in the data will ultimately be captured in the posterior distributions of the fitted parameters. So, the posterior distributions will capture both aleatory and epistemic uncertainties. Calibration studies are known to face the challenge of identifiability, where it is difficult to distinguish between sources of uncertainty [46]. Given this, the value of employing an inference procedure which separates sources of uncertainty with the low-fidelity ET model and the low-resolution parameters of apparent absorptivity and porosity is not clear. Thus, given the known inadequacy of the ET model, we do not attempt to address in depth the identifiability issue in this study, and leave this matter for subsequent investigations.

We choose to separate inference for the depth and width for two reasons. First, the physical processes of interest captured by the calibration of η and ϕ differ along the depth and width. As observed by Kennedy and O’Hagan [44], no computer model can ever perfectly represent the underlying physical process of interest, and so there is always discrepancy between the output of the computer model and the true mean value of the physical process of interest. Then, one can think of calibration studies as inferring missing information about the physical process not captured by the computer model and summarizing this information in inferred parameters, along with any remaining variation in the data due to unreported parameters or aleatory variation. As mentioned, the ET model is known to not capture phenomena in LPBF such as Marangoni convection and recoil pressure, which differ along the depth and width. So, for accurate prediction, it is thus necessary to separate inference. This is supported

by prior studies. Using high-fidelity simulations, Khairallah et al. [6] observed that the melt pool depth is more sensitive to changes in absorptivity than the melt pool width, which is governed more by changes in beam size. They noted that this may be due to the metal vapor plume forming along the melt pool depth, which affects the laser absorption along the melt pool depth. Thus, we expect a different dependence of the absorptivity along the depth with respect to power versus the absorptivity along the width with respect to power. In addition, following the argument by Whalen et al. [23] that the apparent porosity parameter can act as a surrogate for the influence of the localized vapor depression within the melt pool, we expect the dimension of depth to exhibit increased sensitivity to the apparent porosity parameter. Since the width formation is primarily governed by different thermal phenomena, the depth-fit porosity parameter will not capture the same processes as for the width. Kamara et al. [47] studied the inclusion of anisotropic thermal conductivity enhancement and found that an enhancement factor in the the direction of depth was not helpful in modeling the thermal field, but found that enhancement factors in the other two orthogonal directions were required. Since porosity can be viewed as a parameter capturing these heat transfer processes, this also suggests that porosity should differ along the depth and the width to obtain accurate prediction.

Second, it is more computationally tractable to focus on modeling single-output functions. While it is possible to perform multi-objective calibration, this scenario is more complicated. Additionally, Kennedy and O’Hagan [44] focus on the scenario of single-output models. Modeling each dimension separately gives additional flexibility in modeling the effects of phenomena not explicitly incorporated in the ET model, such as the aforementioned vapor depression.

To complete the specification of the calibration procedure, we define the priors for the unobserved parameters. We use Gaussian priors for both the absorptivity and the porosity. Powder absorptivity measurements for the materials considered in our work are available in the literature from Boley et al. [48] and are used to specify the means of the priors. The mean values of the priors are listed in Table 2. However, given the lower fidelity of the ET Model and the different physics governing the the depth and width of the melt pool, the apparent absorptivity parameter η likely does not correspond exactly to powder measurements. Thus, we opt to employ a fairly diffuse Gaussian prior for the absorptivity priors, setting its standard deviation to $\sigma_\eta = 0.15$. For the case of the porosity parameter, some powder bed packing density measurements are available in the literature [49], but unlikely to fully describe the experimental conditions as full details of powder conditions are usually not reported, and the process of spreading powder for AM can be considered as a complex and random process [50]. Due to this, we follow previous work in Whalen et al. [23] and set the mean of the porosity prior to $\mu_\phi = 0.4$ based on the theoretical packing limit of around 64% for equal spheres. We again employ a relatively diffuse prior, setting the standard deviation of $\sigma_\phi = 0.10$. For a given material, we use the same priors for the depth and width models.

To perform inference via MCMC, we use the Metropolis-Hastings algorithm as implemented in the `BayesianTools` R package [51]. We set the burn-in to 500 and draw a total of 10500 samples for each run. We will denote the model parameters as being approximated by the chain values. This is the vector of samples drawn through MCMC, e.g. $\phi_d \approx [\phi_d^{(1)}, \dots, \phi_d^{(K)}]$, where K denotes the total number of samples *after* discarding samples from the burn-in period; i.e. $K = 10000$.

We compiled a dataset of melt pool measurements from multiple literature sources to use for the calibration routine, which are listed in Table 3. Further information about the data may be found in the Supplemental Material, Section S1.

Material	μ_η	σ_η
SS316L	0.68	0.15
IN625	0.67	0.15
IN718	0.67 (*)	0.15
Ti6Al4V	0.74	0.15

(*) Used the measurement for IN625.

Table 2. Mean of the absorptivity priors for the materials studied. Retrieved from Boley et al. [48]

Material	References
IN625	[52]
IN718	[52]
SS316L	[53] [54] [55] [13]
Ti6Al4V	[56] [57] [58] [18]

Table 3. Sources for melt pool geometry data used in parameter calibration.

2.3 Inferring functional dependence of absorptivity and porosity on processing conditions

When the standard Bayesian calibration procedure is applied directly to the entire data set, the functional dependence of unobserved parameters on predictor variables cannot be inferred. That is, parameters to be inferred are assumed to be constant with respect to the predictor variables. For LPBF, this assumption is sub-optimal for fully describing the melt pool formation. Experimental evidence indicates that absorptivity varies with respect to laser power and laser speed [19, 20], and it is reasonable that the apparent porosity can vary with respect to processing parameters that govern keyhole formation (Section 2.2). Besides, from the viewpoint of calibration, the inference of functional dependencies can correct for systematic model error, replacing the $\delta(x)$

discrepancy function in the Kennedy and O’Hagan framework [44, 59] while providing better physical contextualization of the performance and limitations of the model. Thus, rather than inferring η and ϕ which do not vary with respect to the processing inputs X , we aim to infer functions $\eta(X)$ and $\phi(X)$. To do so, it is necessary to *partition* the calibration dataset \mathbb{D} into non-overlapping parts $\mathbb{D}_1, \dots, \mathbb{D}_N$.

In the present work, we achieve such a partitioning by dividing \mathbb{D} into $N = 16$ parts by first binning the data into four parts with equal numbers of data points according to the quartiles of the laser power. Then, for each of these four parts, we then compute the quartiles of the laser speed within that part, and divide a single part into another four parts by binning the data according to the laser speed quartiles. Due to insufficient quantity of data at differing beam diameters, beam diameter is not selected as a binning variable. Then, for each part \mathbb{D}_j , we carry out the inference procedure described in Section 2.2 and obtain the parameter estimates for that part, which we will denote as $\phi_{d,j}, \eta_{d,j}, \phi_{w,j}$, and $\eta_{w,j}$.

In order to obtain estimates for all parameters for an arbitrary X , we use a probabilistic regression model known as HBART (Heteroscedastic Bayesian Additive Regression Trees) [60] as implemented in the R package `rbart` [61]. HBART is a flexible tree-based nonparametric Bayesian regression model which is capable of modeling a variety of functions. Given predictor variable X and output variable Y , it models the conditional distribution $Y | X$ and can estimate the conditional mean and variance, $\mathbb{E}[Y | X]$ and $\text{Var}[Y | X]$. Notably, HBART is a *heteroscedastic* modeling technique, meaning the predictive uncertainty may vary with respect to the predictor variables. This is a realistic property of our current setting; the uncertainty is expected to be small in regions of processing space which have been sampled extensively, but larger in unexplored regions.

We train an HBART model by using the values from the MCMC samples. We prepare the MCMC sample data for usage with HBART in the following manner. Let θ be a calibration parameter, and let $|\mathbb{D}_j| = n_j$ denote the number of data points in the j th part. Let $P_{j,i}, v_{j,i}$ refer to the power and speed of the i th data point in the j th partition. Recall that K denotes the length of the sampled chain after burn-in, i.e. $K = 10000$.

1. For each part \mathbb{D}_j with $1 \leq j \leq n$:

Get the parameter estimate for that part: $\theta_j \approx [\theta_j^{(1)}, \dots, \theta_j^{(K)}]$.

Thin the MCMC samples by selecting every T samples, i.e. $\theta_{j,thin} \approx [\theta_j^{(T)}, \theta_j^{(2T)}, \dots, \theta_j^{(K/T)}]$.

Compute the average value of the processing parameters ($X = [P, v]$) for the part, which we denote \bar{X}_j , and compute as

$$\bar{X}_j = \left[\frac{1}{n_j} \sum_i^{n_j} P_{j,i} \quad \frac{1}{n_j} \sum_i^{n_j} v_{j,i} \right]$$

We can rewrite the final vector with each component as $\bar{X}_j = [\bar{P}_j, \bar{V}_j]$

Pair the thinned samples θ with the mean of that part to yield a dataset $\mathbb{H}_j = \{(\bar{X}_j, \theta_j^{(kT)})\}_{k=1}^{\lfloor K/T \rfloor}$.

- Combine the \mathbb{H}_j back into one dataset \mathbb{H} , i.e. $\mathbb{H} = \bigcup_{j=1}^N \mathbb{H}_j$.
- Fit an HBART model to the dataset \mathbb{H} using the \bar{X}_j as the predictor and θ as the response variable, yielding estimates for the conditional mean and variance of θ : $\mathbb{E}[\theta | X]$ and $\text{Var}[\theta | X]$.

We repeat this process and obtain HBART models for all parameters, which we may write as $\phi_d | X, \phi_w | X, \eta_d | X$, and $\eta_w | X$. Thinning serves to reduce autocorrelation in the chain sample data and improve predictive capability. We set $T = 250$ in our fitting procedure.

2.4 Forward prediction via polynomial chaos expansions

After obtaining a probabilistic model of the inferred parameters' dependence on the processing parameters via HBART, the next step is to use the inferred parameters to obtain estimates of the melt pool geometries using the modified ET Model. We do this via the polynomial chaos method as implemented in the `chaospy` Python package [62].

Polynomial chaos expansions (PCE) are a computationally efficient method for performing uncertainty propagation. Broadly, PCE techniques may be used to solve problems of the following form: find the distribution of Y where $Y = f(X, Q)$, X is a vector of known deterministic inputs, and Q is a vector of stochastic inputs with known distribution. More details can be found in the paper for the `chaospy` package [62].

We apply PCE to our setting to propagate uncertainties from the HBART model of the calibrated parameters into melt pool predictions for both depth and width. Here, our function is ET_d or ET_w , and the deterministic inputs are the processing inputs P, V, σ . Our stochastic inputs are the calibrated parameters ϕ_d, η_d , for the case of computing ET_d and ϕ_w, η_w for the case of computing ET_w . For both width and depth, we model the absorptivity η as a normal distribution with mean $\mathbb{E}[\eta | X]$ and variance $\text{Var}[\eta | X]$ as computed by HBART. However, we model ϕ as a truncated normal distribution between 0 and 1 to avoid numerical errors from the modified ET model. To compute the coefficients of the polynomial expansion, we use the Gaussian quadrature rule as implemented in `chaospy`, which proposes a set of nodes in the parameter domain for the ET model to evaluate. The discretized Stieltjes procedure is used to construct the orthogonal polynomial expansion, and we use a 3rd order expansion.

We perform Monte-Carlo uncertainty propagation as a baseline to ensure the correctness of the PCE-based uncertainty propagation procedure and to inspect the form of the underlying distribution. As discussed in the Supplemental Material, Section S3, the distribution of d and w is well approximated by a normal distribution, enabling the usage of standard techniques for sampling from and modeling normal random variables.

2.5 Defect criteria and printmaps

Empirical criteria to classify melt pools as keyhole or lack-of-fusion have been used in previous computational and experimental studies for mapping out LPBF processing space [3]. For example, Johnson used the criterion $w/d < 1.5$ to identify keyholing melt pools. The criterion $d/t < 1.5$ (where t is the powder bed layer thickness) was used to identify lack-of-fusion melt pools [26]. Given a thermal model capable of predicting these quantities from processing conditions, the expected defect associated with a particular processing condition can be predicted. However, if the thermal model used to predict these quantities is deterministic, then these criteria give a binary prediction - either there is a defect or not. A model incorporating uncertainty, as in the current work, enables the prediction of the probability that a defect will occur given the knowledge from the current experimental data.

Thus, we compute probabilities for the keyholing and lack-of-fusion defects using the criteria above, and treat melt pools which have a low probability of keyholing and lack-of-fusion to be desirable melt pools. To compute the lack-of-fusion probability, i.e. $\mathbb{P}[d/t < 1.5]$, we may rewrite the probability as $\mathbb{P}[d < 1.5t]$ and use the cumulative density of d under the assumption that it is normally distributed. To compute the keyholing defect probability ($\mathbb{P}[w/d < 1.5]$) we use a standard Monte-Carlo approach, i.e. draw samples from the distributions of d and w , compute the expression inside the brackets, and divide the number of samples satisfying the inequality by the total number of samples. Then, these probabilities can be computed over a regular grid in the LPBF processing space in order to map out the keyhole and lack of fusion regions. This information is summarized in a contour map of probabilities, which we call the probabilistic printability map.

3 Results and discussion

3.1 Melt pool geometry predictions without calibration

To assess the capabilities of the modified ET Model before calibration, we predicted melt pool geometries for all parameter combinations in the respective materials' datasets. The prior means were used for the absorptivity and porosity parameter values, and the resulting R^2 values may be found in Table 4. Additional plots may be found in the Supplemental Material, Section S4. The modified ET model tends to under-predict the depth and over-predict the width (Figure 2). This is consistent with observations from previous applications of the ET model in LPBF [26].

3.2 Fitted absorptivity and comparison with experimental measurements

We observed that the predicted means for the depth-fit absorptivity (η_d) and the depth-fit porosity (ϕ_d) tended to increase with respect to power and decrease with respect to speed for all materials. Depth-fit porosity and absorptivity tend to saturate past a certain power threshold. This general behavior is consistent with experimental work and cor-

Material	Depth R^2	Width R^2
IN625	0.804	0.769
IN718	0.848	0.815
SS316L	0.766	0.747
Ti6Al4V	0.596	0.584

Table 4. R^2 values for prediction from modified ET Model before calibration. Absorptivity and porosity were set to their prior values (Section 2.2).

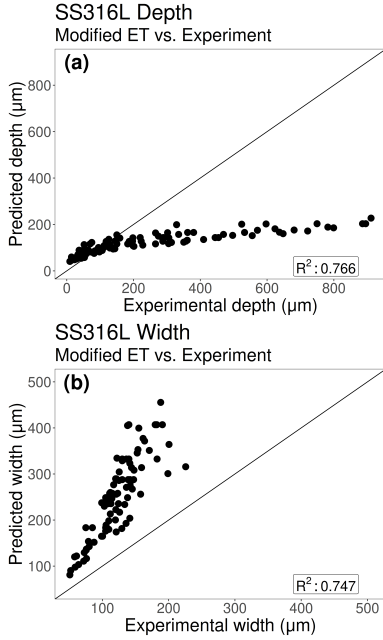


Fig. 2. Uncalibrated predictions for SS316L from the modified ET model against available data for calibration (Table 3). (a) compares the predicted depth against the experimental depth, (b) compares the predicted width against the experimental width. Both plots exhibit systematic discrepancy with experiment. The depth is under-predicted and the width is over-predicted, which has been observed in prior applications of the ET model (e.g Johnson et al. [26])

responds to a the physics of the melt pool. Ye et al. [19] observed absorptivity saturates at a certain threshold. An increase and saturation in the fitted porosity corresponds to the formation of the vapor depression, indicating the onset of the keyholing mode and increasing depth. However, the width-fit absorptivity η_w and the width-fit porosity ϕ_w were often nearly constant, suggesting the validity of constant parameter values for computing the width. This is in agreement with the observation by Khairallah et al. [6] that the melt pool width is less sensitive to changes in absorptivity, indicating a constant absorptivity and porosity may be sufficient to capture the relevant physics. The vapor depression primarily affects the dimension of depth, and the width is more sensitive to the beam diameter. Notable exceptions were the absorptivity functions ϕ_w for Ti6Al4V and SS316L. The fitted ϕ_w for these materials tended to decrease with respect to power, but

did not vary significantly with respect to speed. This behavior was not observed for IN625 and IN718. It is possible this behavior may be correlated to heat transfer modes not in the ET model such as Marangoni convection [63], which is known to affect the formation of the melt pool width [64]. However, due to the large uncertainties, no conclusive statement can be made about what this observation might indicate. Plots of absorptivity and porosity for all materials can be found in the Supplemental Material, Section S5.

We compare the predicted depth-fit absorptivity from SS316L to the experiment by Trapp et al. [20] (Figure 3). We find that the mean predicted absorptivity follows the data from Trapp et al. well. We also compare the predicted depth-fit absorptivity from Ti6Al4V to the experiment by Ye et al. [19]. We find that the experimental measurement from Ye et al. lies within the 95% credible region predicted by our model. The good correspondence indicates that our inference procedure has managed to capture the relevant physical dynamics in the LPBF process. However, the uncertainty is large. This may arise due to the approach of partitioning, which effectively models regions of process space independently from each other during inference. Thus, information about the value of the parameter is not shared between partitions during inference, resulting in inefficient estimation.

In contrast, we find the model systematically under-predicts the absorptivity measurement for IN625 by Lane et al. [65] This may be due to the discrepancy between the beam diameters considered in the calibration data versus the beam diameter in the experiment by Lane et al., which will be discussed in Section 3.3. In addition, Lane et al. employed a photoreflectometer approach for measuring the laser energy absorption, in comparison to Trapp et al. and Ye et al. who utilized calorimetric methods. Lane et al. noted that discrepancies may arise between these approaches, e.g laser energy may be scattered and not absorbed into the workpiece.

3.3 In-sample and out-of-sample fit for melt pool predictions after calibration

We assessed the performance of the model by using the HBART fit parameter curves to assess the in-sample (i.e training data) and out-of-sample fit of the calibrated ET model to melt pool geometry data. For the in-sample data, there is a moderate improvement for all materials in R^2 fit values for the depth, and the predictions qualitatively exhibit improved agreement with the experimental data and deviate less systematically. We compute the coverage statistic, denoting the percentage of points from the experimental dataset which fall within the 95% credible region given by our prediction routine. In ideal circumstances, this should be near 95%. However, we find that the depth predictions exhibit coverage values of around 75-85%, indicating a possible under-prediction of uncertainty. This may be due to systematic deviation from the mean not yet accounted for by our modeling technique. This is most apparent for Ti6Al4V, which may be due to the heterogeneity of the data. In contrast, the width coverage is consistently near 100% for all materials, indicating that the uncertainty may be over-

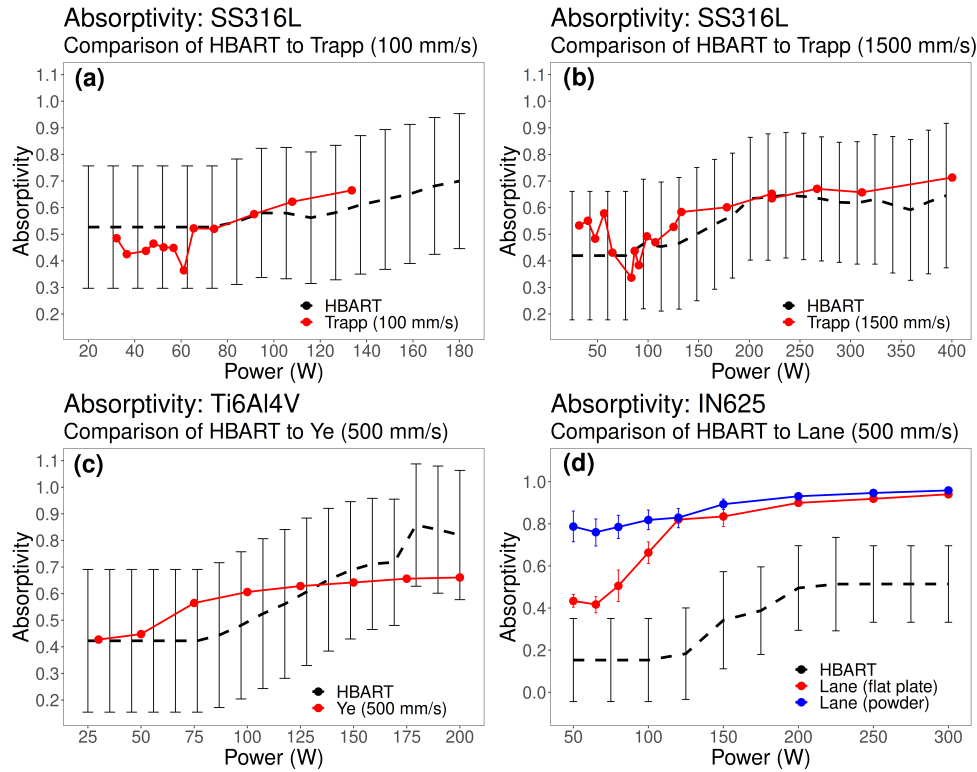


Fig. 3. Comparison of experimentally measurement laser absorption vs. absorption predicted by HBART model. (a), (b) HBART predicted absorptivity compared to the experimentally measured absorptivity reported by Trapp et al. for the 316L stainless steel [20]. (a) Comparison of absorptivity for a constant scanning speed of 100 mm/s. (b) Comparison of absorptivity for a constant scanning speed of 1500 mm/s. (c) HBART predicted absorptivity compared to the experimental work of Ye et al. for Ti6Al4V [19]. The red line is the average absorptivity across powder layer thicknesses from Figure 1C in Ye et al. (d) HBART predicted absorptivity compared to the experimental work of Lane et al. for IN625 [65]. There is a large discrepancy between the predicted and experimental results. However, the predicted curve seems to follow approximately the same shape as the Lane et al. data.

predicted. Additional plots for in-sample predictions can be found in the Supplemental Material, Section S6.

Material, Section S7.

Material	Fitted R^2		Coverage	
	Depth	Width	Depth	Width
IN625	0.87	0.918	84.4%	100%
IN718	0.885	0.868	88.9%	97.8%
SS316L	0.832	0.752	81.4%	100%
Ti6Al4V	0.646	0.833	76.6%	97.7%

Table 5. R^2 values for prediction on in-sample data from modified ET Model with calibrated absorptivity and porosity.

Material	Fitted R^2		Coverage	
	Depth	Width	Depth	Width
IN625 (Dilip) [66]	0.849	0.848	72.7%	97%
IN625 (Lane) [65]	0.971 (*)	0.833	44.4%	100%
IN718 (Lee) [52]	0.765	0.908	80%	100%
Ti6Al4V (Liu) [67]	0.903	0.909	57.7%	100%

(*) Strong linear relationship despite poor fit.

Table 6. R^2 values for prediction on out-of-sample data from modified ET Model with calibrated absorptivity and porosity.

We test the predictive capabilities of our model by predicting on out-of-sample data. Melt pool geometries for IN625 were retrieved from Dilip et al. [66] and Lane et al. [65]; and melt pool measurements for Ti-6Al-4V were retrieved from Liu et al. [67]. An additional dataset for Lee et al. [52] for IN718 as manufactured on a Mlab machine was also used to test the model. The R^2 and coverage of the model are tabulated in Table 6. Additional plots and information about the data can be found in the Supplemental

Performance of the model is good on the test datasets, achieving R^2 values roughly around 0.8. (See Table 6 and Figure 4.) The model is able to capture the essential correlations between processing parameters and melt-pool geometry present in the data, and the model is able to achieve good predictive performance for out-of-sample data with similar conditions. Thus, it is sufficient for exploration of the process space. However, it is interesting to investigate possible reasons for the poorer performance of the model on the

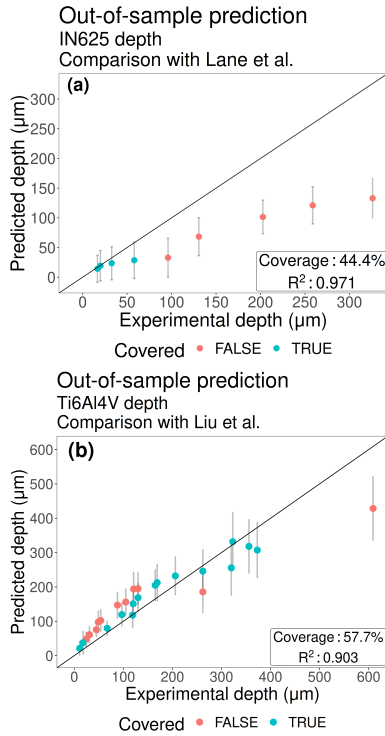


Fig. 4. Comparison of predicted depths from modified ET model to out-of-sample experimental depths. (a) shows the comparison of predictions for IN625 with Lane et al. [65]. There is a large discrepancy between experiment and prediction. Despite this, a high R^2 is achieved due to a strong correlation. (b) shows the comparison with Liu et al. [67], which shows good agreement. One experimental point with a larger depth is under-predicted.

IN625 data from Lane et al. to understand the limits of the model. One possible explanation is the lack of information in the model regarding how laser energy absorption changes with respect to beam diameter, as observed by Ye et al. [19]. Since this relationship is not modeled within the ET model, it is to be inferred via calibration. But, this is not captured well in the current framework due to a lack of extensive data for multiple beam diameters. In particular, we found that including beam diameter as a feature in the HBART model does not improve the predictive performance (See Supplemental Material, Section S2.)

Thus, we can view the inferred parameters as being applicable to a specific range of beam diameters, namely the average of those present in the calibration data. For example, the original Lee et al. [52] data contained beam diameters of 50, 100, and 150 μm . Thus, the calibrated model performed reasonably well on the Dilip et al. data, which employed a beam diameter of 100 μm . In contrast, Lane et al employed a beam diameter of 62 μm , indicating a more focused beam with more energy absorption, and so our model systematically underpredicts the melt pool depth in this scenario.

The results in this section demonstrate the dependence of inferred parameters on the overall composition of the dataset. Ideally, clean data with appropriately selected processing parameters will give the best predictive results for

a variety of conditions. Even so, with limited experimental data, the model is able to capture useful correlations in the LPBF process that can be used to explore a processing regime of interest.

3.4 Probabilistic printability maps and comparison with experimental printability map

To demonstrate the descriptive power of the model, we compute printmaps for all materials investigated within the processing region of the experimental data. Each point from the experimental dataset is labeled by computing the defect criterion using experimental melt pool geometry measurements, and plotted on top of the printmap. We find that for the materials investigated, the printmap is able to capture the essential boundaries present in the data. Figure 5 shows the printmaps for IN625 and IN718 overlaid with the labeled in-sample calibration data. The calibration data is labeled by computing the same defect criteria, but using experimental melt pool geometries rather than simulated ones. The maps for both the keyhole and lack of fusion defect illustrate clear transition regions, where a region of high probability smoothly transitions to a region of low probability. Additional printability maps for the other materials are available in the Supplemental Material, Section S8. While the IN625 and IN718 printability maps are well structured with clear keyhole and lack-of-fusion zones, there were data challenges with other printmaps that led to difficulties in modeling. For example, the Ti6Al4V map overpredicts the keyhole region to the measurement technique by Vaglio et al. [56] where the width is taken to be the width of the melt track, rather than the width of the melt pool. However, despite the data challenges, the printability maps tend to accurately summarize the trends present in the experimental data, indicating that if given clean and accurate data, the model will describe the trends in the data well. From a practical standpoint, this uncertain boundary is expected to assist process engineers in setting appropriate risk tolerances for their choice of processing parameters based on the current data. Alternately, this transition region may be a region of interest for further targeted experimentation in order to fully understand the inherent variabilities in the keyhole-conduction transition.

We assess the predictive capability of the model by computing the printmap for regions of process space where no training data exist, and validate the prediction with literature data. We compare the generated printmap for IN718 to the data from Scime and Beuth [5], which characterizes a larger region of processing space than present in our calibration data. The comparison is illustrated in Figure 6. We find that the model is able to generalize into regions of processing space in which it has no data for IN718 reasonably well, and captures the essential boundaries between keyholing-conduction and conduction-lack-of-fusion well based upon the Scime and Beuth data. In the keyhole map, near the boundaries of the processing space and in regions where no training data exist, we see that the model outputs probabilities near 0.5, indicating larger predictive uncertainty. This area of increased predictive uncertainty

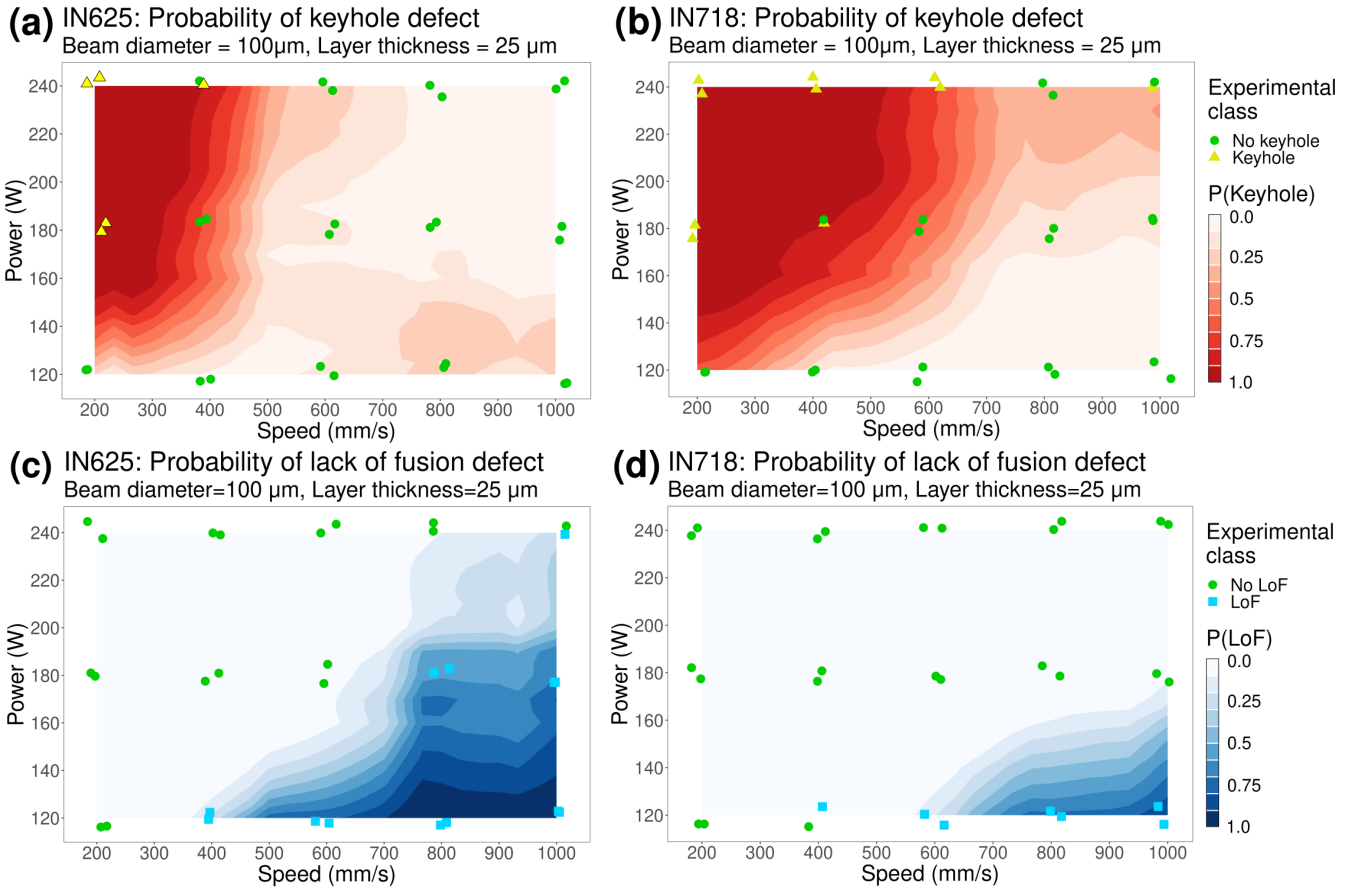


Fig. 5. Probabilistic printability maps for IN625 and IN718. The data used for calibration is labeled by computing the defect criterion using the experimental measurements, and overlaid on top of the printmap computed by the ET model. “P(Keyhole)” and “P(LoF)” denote the probability of the keyhole defect and the lack of fusion defect, respectively. (a),(c) are the probabilistic printability maps for IN625, computed with a beam diameter of $100\ \mu\text{m}$ and a layer thickness of $25\ \mu\text{m}$. (b),(d) are the probabilistic printability maps for IN718, computed for the same conditions as IN625. (a),(b) presents the probability of keyholing as a function of power of speed, and (c),(d) presents the probability of lack of fusion as a function of power and speed. The calibration data from Lee et al. [52] is overlaid on both plots. The color and shape of the markers correspond to the characterization of the Lee et al. data according to the the geometric defect criteria as computed on the experimental dataset. Some noise is added to the power and speed for the IN625 and IN718 data in order to display replicated measurements. Both the keyholing and lack of fusion maps have well-defined regions and capture the boundaries present in the Lee et al. data. The lack of fusion region for IN718 is smaller than IN625, and the keyhole region for IN718 appears to be larger than for IN625.

is more apparent in the high-power high-speed region (upper right corner) of the keyhole map (Figure 6a). Here, the probability appears greater in the high-power high-speed region than in the low-power high-speed region. This makes intuitive physical sense as the probability of keyholing increases with power, but the model is uncertain due to the lack of data. In the lack-of-fusion maps, this increase in predictive uncertainty is seen as the boundary region between lack-of-fusion-free region and the lack-of-fusion region becomes wider near higher speeds and higher powers (Figures 6b and 6c.) This increased uncertainty is likely due to a lack of data in the region. However, Wang et al. [22] observed a similar trend where the variability of lack-of-fusion porosity increased with respect to speed. It is possible our model may have captured a similar trend, but further investigation is required to verify.

Scime and Beuth provided a value of $70\ \mu\text{m} \pm 20\ \mu\text{m}$ for the layer-thickness. We find that given our model, a value

of $70\ \mu\text{m}$ results in the over-prediction of the lack-of-fusion region, i.e some points marked as conduction fall within the lack-of-fusion region. Using a layer thickness value of $50\ \mu\text{m}$ appears to better match the experimental characterization from Scime and Beuth. This over-prediction may be due to underprediction of the mean melt pool depth.

4 Summary and conclusion

A probabilistic modeling technique for identifying regions of process space likely to result in defect-free products based upon melt pool geometry criteria was developed. We utilized the modified ET model, incorporating both temperature-dependent thermophysical properties and the additional parameters of powder bed porosity and laser absorptivity. The modified ET model was calibrated against melt pool measurement data from the literature by using a Bayesian inference procedure to infer the values of laser ab-

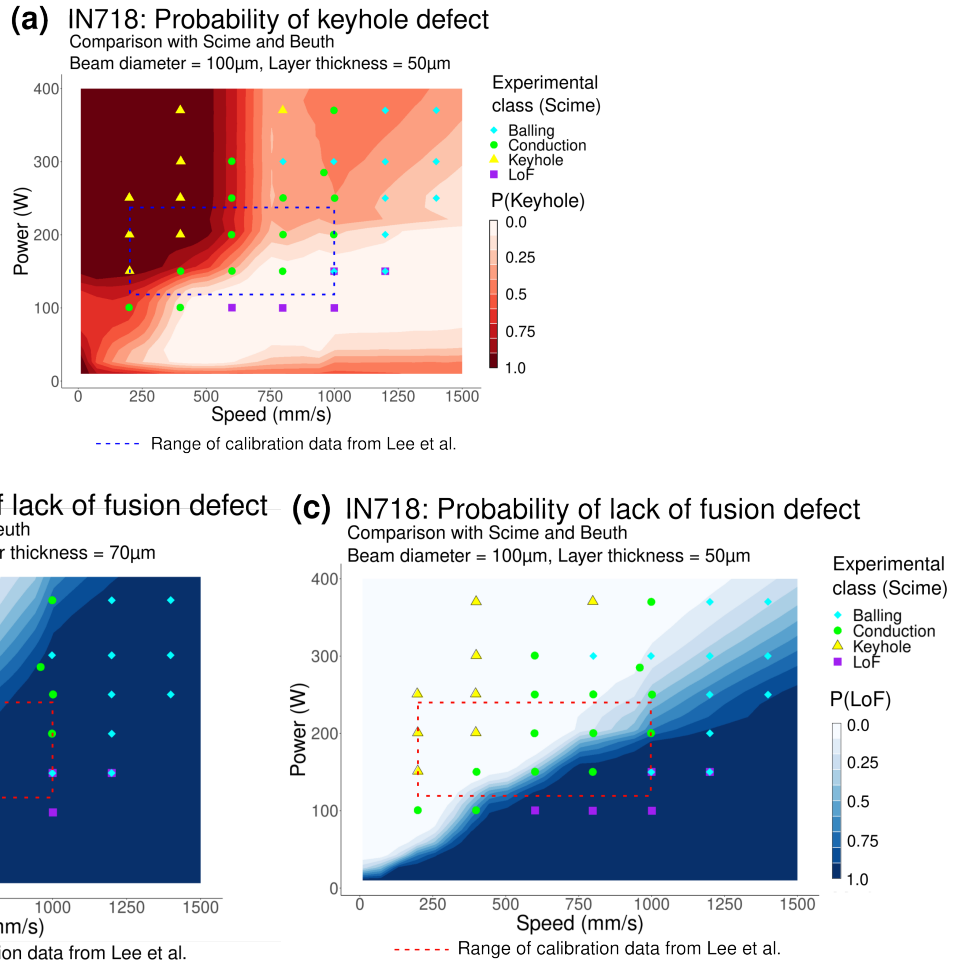


Fig. 6. Comparison of the created probabilistic printmap for IN718 with the experiment by Scime and Beuth [5]. The shape and color of the overlaid markers represent the experimental characterization by Scime and Beuth [5], who use similar geometry-based criteria. The blue box with dotted lines indicates the range of processing parameters containing the data used for calibration (Lee et al. [52]). “P(Keyhole)” and “P(LoF)” denote the probability of the keyhole defect and the lack of fusion defect, respectively. **(a)** displays the keyhole printability map for IN718. The keyhole region is well-defined and captures the boundary in the Scime and Beuth data. At higher powers where no calibration data is available, the predicted probability is near 0.5, indicating a large amount of predictive uncertainty. This also occurs near the bottom edge of the processing space. **(b)** shows the lack of fusion printability map for IN718, computed with the nominal layer thickness of 70 µm. The lack of fusion region is over-predicted and does not match as well with the characterization by Scime and Beuth using this layer thickness value. **(c)** shows the lack of fusion printability map for IN718, computed with a layer thickness of 50 µm, which falls within the layer thickness reported by Scime and Beuth of 70 µm ± 20 µm, which appears to better align with the lack of fusion characterization by Scime and Beuth.

sorptivity and powder porosity. However, rather than inferring values for these parameters which do not vary with respect to processing conditions, we infer functional relationships for absorptivity and porosity which vary with respect to laser power and scan speed. This was done by partitioning the dataset, inferring values for each partition via MCMC, and fitting an HBART model to the MCMC samples. Then, the fitted parameters were used to produce probabilistic predictions of the melt pool geometry. Computation of these probabilistic predictions was facilitated by the use of the polynomial chaos technique. These probabilistic predictions were used to create probabilistic printability maps, which more realistically capture uncertainties about the inherent stochasticity in LPBF and current knowledge given the limited experimental data.

Our key findings are:

1. *Inference of absorptivity.* The absorptivity curves inferred via the calibration procedure match well to experiments conducted under similar processing conditions to the calibration data.
2. *In-sample and out-of-sample fit.* The calibration procedure improved the fit of the modified ET model to the calibration data. The model was capable of accurately predicting melt pool geometries on out-of-sample data processed under similar conditions to the calibration data.
3. *Printmaps.* The calibrated model was capable of generating printmaps which correctly identified the transition regions in LPBF process space based on experiment, and

was capable of generalizing to larger process spaces in which the model was not trained.

4. *Quantification of uncertainty.* Experimental width measurements nearly always fell within the error bars predicted by the model, whereas in cases not exhibiting systematic deviation from experiment, roughly 70%-80% of experimental depth measurements fell within the error bars predicted by the model. This suggests that the uncertainty from the depth is likely under-predicted and the uncertainty from the width is over-predicted.
5. *Effect of beam diameter.* The model did not adequately account for the effect of beam diameter on melt pool geometry and absorption, and could only model processing conditions with beam diameters similar to the average beam diameter present in the calibration data.

A source of uncertainty that impacted predictions for SS316L and Ti6Al4V was machine-to-machine variability, and data heterogeneity. It is known that significant differences can arise in specimens manufactured from different machines [2]. Parameters that are not reported or difficult to measure, or differing measurement techniques, causes systematic differences between datasets that are compiled together and used for calibration, adding additional sources of discrepancy within the calibration framework. While the calibrated model could perform reasonably well on the validation test sets, indicating that there are general trends which appear to be applicable from machine-to-machine, one key area to improve the applicability of our framework is to develop additional methods for investigating and quantifying this source of uncertainty. Future work can investigate further improvement by incorporating the influence of beam diameter on absorptivity or the melt pool geometry, either via statistical inference or further modification of the ET model, as well as alternate calibration schemes that better quantify associated uncertainties, e.g by separation of aleatory and epistemic uncertainties.

Overall, this work demonstrates the potential of utilizing parameter calibration and UQ to attain a good and computationally efficient descriptive model capable of mapping out the LPBF process space and summarizing the current knowledge available in experimental data. In addition, we demonstrated that inferring processing-parameter dependent absorptivity and porosity has physical justification and can improve the flexibility and performance of the model. We demonstrated the value of the model by using it to create probabilistic printability maps, which are able to summarize current knowledge about processing space along with the associated uncertainties.

5 Acknowledgment

Authors acknowledge support from the University of Virginia Rivanna high-performance computing cluster for the computational resources. We thank Mr. Daniel Xue for assistance in running some of the simulations.

References

- [1] Yap, C. Y., Chua, C. K., Dong, Z. L., Liu, Z. H., Zhang, D. Q., Loh, L. E., and Sing, S. L., 2015. "Review of selective laser melting: Materials and applications". *Applied Physics Reviews*, **2**(4), Dec., p. 041101. Publisher: American Institute of Physics.
- [2] Reijonen, J., Björkstrand, R., Riipinen, T., Que, Z., Metsä-Kortelainen, S., and Salmi, M., 2021. "Cross-testing laser powder bed fusion production machines and powders: Variability in mechanical properties of heat-treated 316L stainless steel". *Materials & Design*, **204**, June, p. 109684.
- [3] Tang, M., Pistorius, P. C., and Beuth, J. L., 2017. "Prediction of lack-of-fusion porosity for powder bed fusion". *Additive Manufacturing*, **14**, Mar., pp. 39–48.
- [4] Cunningham, R., Narra, S. P., Montgomery, C., Beuth, J., and Rollett, A. D., 2017. "Synchrotron-Based X-ray Microtomography Characterization of the Effect of Processing Variables on Porosity Formation in Laser Power-Bed Additive Manufacturing of Ti-6Al-4V". *JOM*, **69**(3), Mar., pp. 479–484.
- [5] Scime, L., and Beuth, J., 2019. "Melt pool geometry and morphology variability for the Inconel 718 alloy in a laser powder bed fusion additive manufacturing process". *Additive Manufacturing*, **29**, Oct., p. 100830.
- [6] Khairallah, S. A., Anderson, A. T., Rubenchik, A., and King, W. E., 2016. "Laser powder-bed fusion additive manufacturing: Physics of complex melt flow and formation mechanisms of pores, spatter, and denudation zones". *Acta Materialia*, **108**, Apr., pp. 36–45.
- [7] Eagar, T., Tsai, N., et al., 1983. "Temperature fields produced by traveling distributed heat sources". *Welding journal*, **62**(12), pp. 346–355.
- [8] Rosenthal, D., 1946. "The Theory of Moving Sources of Heat and Its Application to Metal Treatments". *Transactions of the American Society of Mechanical Engineers*, **68**(8), Nov., pp. 849–865.
- [9] Seede, R., Shoukr, D., Zhang, B., Whitt, A., Gibbons, S., Flater, P., Elwany, A., Arroyave, R., and Karaman, I., 2020. "An ultra-high strength martensitic steel fabricated using selective laser melting additive manufacturing: Densification, microstructure, and mechanical properties". *Acta Materialia*, **186**, Mar., pp. 199–214.
- [10] Promoppatum, P., and Yao, S.-C., 2019. "Analytical evaluation of defect generation for selective laser melting of metals". *The International Journal of Advanced Manufacturing Technology*, **103**(1-4), July, pp. 1185–1198.
- [11] Qin, J., Hu, F., Liu, Y., Witherell, P., Wang, C. C., Rosen, D. W., Simpson, T. W., Lu, Y., and Tang, Q., 2022. "Research and application of machine learning for additive manufacturing". *Additive Manufacturing*, **52**, Apr., p. 102691.
- [12] Tapia, G., Khairallah, S., Matthews, M., King, W. E., and Elwany, A., 2018. "Gaussian process-based surrogate modeling framework for process planning in laser powder-bed fusion additive manufacturing of 316L stainless steel". *The International Journal of Advanced*

- Manufacturing Technology*, **94**(9), Feb., pp. 3591–3603.
- [13] Kamath, C., 2016. “Data mining and statistical inference in selective laser melting”. *The International Journal of Advanced Manufacturing Technology*, **86**(5), Sept., pp. 1659–1677.
- [14] Saunders, R., Rawlings, A., Birnbaum, A., Iliopoulos, A., Michopoulos, J., Lagoudas, D., and Elwany, A., 2022. “Additive Manufacturing Melt Pool Prediction and Classification via Multifidelity Gaussian Process Surrogates”. *Integrating Materials and Manufacturing Innovation*, **11**(4), Dec., pp. 497–515.
- [15] Ning, J., Sievers, D. E., Garmestani, H., and Liang, S. Y., 2019. “Analytical Modeling of In-Process Temperature in Powder Bed Additive Manufacturing Considering Laser Power Absorption, Latent Heat, Scanning Strategy, and Powder Packing”. *Materials*, **12**(5), Jan., p. 808. Number: 5 Publisher: Multidisciplinary Digital Publishing Institute.
- [16] Promoppatum, P., Yao, S.-C., Pistorius, P. C., and Rollett, A. D., 2017. “A Comprehensive Comparison of the Analytical and Numerical Prediction of the Thermal History and Solidification Microstructure of Inconel 718 Products Made by Laser Powder-Bed Fusion”. *Engineering*, **3**(5), Oct., pp. 685–694.
- [17] Honarmandi, P., Seede, R., Xue, L., Shoukr, D., Morcos, P., Zhang, B., Zhang, C., Elwany, A., Karaman, I., and Arroyave, R., 2021. “A rigorous test and improvement of the Eagar-Tsai model for melt pool characteristics in laser powder bed fusion additive manufacturing”. *Additive Manufacturing*, **47**, Nov., p. 102300.
- [18] Patel, S., and Vlasea, M., 2020. “Melting modes in laser powder bed fusion”. *Materialia*, **9**, Mar., p. 100591.
- [19] Ye, J., Khairallah, S. A., Rubenchik, A. M., Crumb, M. F., Guss, G., Belak, J., and Matthews, M. J., 2019. “Energy Coupling Mechanisms and Scaling Behavior Associated with Laser Powder Bed Fusion Additive Manufacturing”. *Advanced Engineering Materials*, **21**(7).
- [20] Trapp, J., Rubenchik, A. M., Guss, G., and Matthews, M. J., 2017. “In situ absorptivity measurements of metallic powders during laser powder-bed fusion additive manufacturing”. *Applied Materials Today*, **9**, Dec., pp. 341–349.
- [21] Hu, Z., and Mahadevan, S., 2017. “Uncertainty quantification and management in additive manufacturing: current status, needs, and opportunities”. *The International Journal of Advanced Manufacturing Technology*, **93**(5-8), Nov., pp. 2855–2874.
- [22] Wang, Z., Jiang, C., Liu, P., Yang, W., Zhao, Y., Horstemeyer, M. F., Chen, L.-Q., Hu, Z., and Chen, L., 2020. “Uncertainty quantification and reduction in metal additive manufacturing”. *npj Computational Materials*, **6**(1), Nov., pp. 1–10. Number: 1 Publisher: Nature Publishing Group.
- [23] Whalen, B. J., Ma, J., and Balachandran, P. V., 2021. “A Bayesian Approach to the Eagar-Tsai Model for Melt Pool Geometry Prediction with Implications in Additive Manufacturing of Metals”. *Integrating Materials and Manufacturing Innovation*, **10**(4), Dec., pp. 597–609.
- [24] von Toussaint, U., 2011. “Bayesian inference in physics”. *Reviews of Modern Physics*, **83**(3), Sept., pp. 943–999. Publisher: American Physical Society.
- [25] Tapia, G., King, W., Johnson, L., Arroyave, R., Karaman, I., and Elwany, A., 2018. “Uncertainty Propagation Analysis of Computational Models in Laser Powder Bed Fusion Additive Manufacturing Using Polynomial Chaos Expansions”. *Journal of Manufacturing Science and Engineering*, **140**(12), Oct.
- [26] Johnson, L., Mahmoudi, M., Zhang, B., Seede, R., Huang, X., Maier, J. T., Maier, H. J., Karaman, I., Elwany, A., and Arroyave, R., 2019. “Assessing printability maps in additive manufacturing of metal alloys”. *Acta Materialia*, **176**, Sept., pp. 199–210.
- [27] Agrawal, A. K., Rankouhi, B., and Thoma, D. J., 2022. “Predictive process mapping for laser powder bed fusion: A review of existing analytical solutions”. *Current Opinion in Solid State and Materials Science*, **26**(6), Dec., p. 101024.
- [28] Vela, B., Mehalic, S., Sheikh, S., Elwany, A., Karaman, I., and Arroyave, R., 2022. “Evaluating the intrinsic resistance to balling of alloys: A High-throughput physics-informed and data-enabled approach”. *Additive Manufacturing Letters*, **3**, Dec., p. 100085.
- [29] Ye, J., Vaughan, M., Karaman, I., Arroyave, R., and Elwany, A., 2022. “A New Efficient Printability Assessment Framework for Directed Energy Deposition Processes: A Response Surface Method Approach”. *IIE Annual Conference. Proceedings*, pp. 1–6. Num Pages: 1-6 Place: Norcross, United States Publisher: Institute of Industrial and Systems Engineers (IISE).
- [30] Pal, R., 2008. “On the Lewis-Nielsen model for thermal/electrical conductivity of composites”. *Composites Part A: Applied Science and Manufacturing*, **39**(5), May, pp. 718–726.
- [31] Chen, S., and Saxena, S., 1975. “Thermal conductivity of argon in the temperature range 350 to 2500 K”. *Molecular Physics*, **29**(2), Feb., pp. 455–466. Publisher: Taylor & Francis eprint: <https://doi.org/10.1080/00268977500100391>.
- [32] Hoshino, T., Mito, K., Nagashima, A., and Miyata, M., 1986. “Determination of the thermal conductivity of argon and nitrogen over a wide temperature range through data evaluation and shock-tube experiments”. *International Journal of Thermophysics*, **7**(3), May, pp. 647–662.
- [33] Nikam, S. H., Quinn, J., and McFadden, S., 2021. “A simplified thermal approximation method to include the effects of Marangoni convection in the melt pools of processes that involve moving point heat sources”. *Numerical Heat Transfer, Part A: Applications*, **79**(7), Apr., pp. 537–552.
- [34] Kaschnitz, E., Kaschnitz, L., and Heugenhauer, S., 2019. “Electrical Resistivity Measured by Millisecond

- Pulse Heating in Comparison with Thermal Conductivity of the Superalloy Inconel 625 at Elevated Temperature”. *International Journal of Thermophysics*, **40**(3), Feb., p. 27.
- [35] Moges, T., Yang, Z., Jones, K., Feng, S., Witherell, P., and Lu, Y., 2021. “Hybrid Modeling Approach for Melt-Pool Prediction in Laser Powder Bed Fusion Additive Manufacturing”. *Journal of Computing and Information Science in Engineering*, **21**(5), May.
- [36] Heugenhauer, S., and Kaschnitz, E., 2019. “Density and thermal expansion of the nickel-based superalloy INCONEL 625 in the solid and liquid states”. *High Temperatures – High Pressures*, **48**(4), July, pp. 381–393. Publisher: Old City Publishing, Inc.
- [37] Weirather, J., Rozov, V., Wille, M., Schuler, P., Seidel, C., Adams, N. A., and Zaeh, M. F., 2019. “A Smoothed Particle Hydrodynamics Model for Laser Beam Melting of Ni-based Alloy 718”. *Computers & Mathematics with Applications*, **78**(7), Oct., pp. 2377–2394.
- [38] Basak, D., Overfelt, R. A., and Wang, D., 2003. “Measurement of Specific Heat Capacity and Electrical Resistivity of Industrial Alloys Using Pulse Heating Techniques”. *International Journal of Thermophysics*, **24**(6), Nov., pp. 1721–1733.
- [39] Pottlacher, G., Hosaeus, H., Kaschnitz, E., and Seifert, A., 2002. “Thermophysical properties of solid and liquid Inconel 718 Alloy*”. *Scandinavian Journal of Metallurgy*, **31**(3), pp. 161–168. eprint: <https://onlinelibrary.wiley.com/doi/pdf/10.1034/j.1600-0692.2002.310301.x>.
- [40] Mills, K. C., 2002. “Ni - IN 718”. In *Recommended Values of Thermophysical Properties for Selected Commercial Alloys*, K. C. Mills, ed., Woodhead Publishing Series in Metals and Surface Engineering. Woodhead Publishing, Jan., pp. 181–190.
- [41] Kim, C. S., 1975. Thermophysical properties of stainless steels. Tech. Rep. ANL-75-55, Argonne National Lab., Ill. (USA), Sept.
- [42] Mills, K. C., 2002. “Fe-304 Stainless Steel”. In *Recommended Values of Thermophysical Properties for Selected Commercial Alloys*, K. C. Mills, ed., Woodhead Publishing Series in Metals and Surface Engineering. Woodhead Publishing, Jan., pp. 127–134.
- [43] Mills, K. C., 2002. “Ti: Ti-6 Al-4 V (IMI 318)”. In *Recommended Values of Thermophysical Properties for Selected Commercial Alloys*, K. C. Mills, ed., Woodhead Publishing Series in Metals and Surface Engineering. Woodhead Publishing, Jan., pp. 211–217.
- [44] Kennedy, M. C., and O’Hagan, A., 2001. “Bayesian calibration of computer models”. *Journal of the Royal Statistical Society: Series B (Statistical Methodology)*, **63**(3), pp. 425–464. eprint: <https://onlinelibrary.wiley.com/doi/pdf/10.1111/1467-9868.00294>.
- [45] van Ravenzwaaij, D., Cassey, P., and Brown, S. D., 2018. “A simple introduction to Markov Chain Monte–Carlo sampling”. *Psychonomic Bulletin & Review*, **25**(1), Feb., pp. 143–154.
- [46] Arendt, P. D., Apley, D. W., and Chen, W., 2012. “Quantification of Model Uncertainty: Calibration, Model Discrepancy, and Identifiability”. *Journal of Mechanical Design*, **134**(10), Sept.
- [47] Kamara, A. M., Wang, W., Marimuthu, S., and Li, L., 2011. “Modelling of the Melt Pool Geometry in the Laser Deposition of Nickel Alloys Using the Anisotropic Enhanced Thermal Conductivity Approach”. *Proceedings of the Institution of Mechanical Engineers, Part B: Journal of Engineering Manufacture*, **225**(1), Jan., pp. 87–99.
- [48] Boley, C. D., Mitchell, S. C., Rubenchik, A. M., and Wu, S. S. Q., 2016. “Metal powder absorptivity: modeling and experiment”. *Applied Optics*, **55**(23), Aug., p. 6496.
- [49] Nguyen, Q. B., Nai, M. L. S., Zhu, Z., Sun, C.-N., Wei, J., and Zhou, W., 2017. “Characteristics of Inconel Powders for Powder-Bed Additive Manufacturing”. *Engineering*, **3**(5), Oct., pp. 695–700.
- [50] Chen, H., Wei, Q., Zhang, Y., Chen, F., Shi, Y., and Yan, W., 2019. “Powder-spreading mechanisms in powder-bed-based additive manufacturing: Experiments and computational modeling”. *Acta Materialia*, **179**, Oct., pp. 158–171.
- [51] Hartig, F., Minunno, F., and Paul, S., 2019. *BayesianTools: General-Purpose MCMC and SMC Samplers and Tools for Bayesian Statistics*. R package version 0.1.7.
- [52] Lee, S., Peng, J., Shin, D., and Choi, Y. S., 2019. “Data analytics approach for melt-pool geometries in metal additive manufacturing”. *Science and Technology of Advanced Materials*, **20**(1), Dec., pp. 972–978. Publisher: Taylor & Francis eprint: <https://doi.org/10.1080/14686996.2019.1671140>.
- [53] Scipioni Bertoli, U., Wolfer, A. J., Matthews, M. J., Delplanque, J.-P. R., and Schoenung, J. M., 2017. “On the limitations of Volumetric Energy Density as a design parameter for Selective Laser Melting”. *Materials & Design*, **113**, Jan., pp. 331–340.
- [54] Goossens, L. R., and Van Hooreweder, B., 2021. “A virtual sensing approach for monitoring melt-pool dimensions using high speed coaxial imaging during laser powder bed fusion of metals”. *Additive Manufacturing*, **40**, Apr., p. 101923.
- [55] Hu, Z., Nagarajan, B., Song, X., Huang, R., Zhai, W., and Wei, J., 2019. “Formation of SS316L Single Tracks in Micro Selective Laser Melting: Surface, Geometry, and Defects”. *Advances in Materials Science and Engineering*, **2019**, Jan., p. e9451406. Publisher: Hindawi.
- [56] Vaglio, E., De Monte, T., Lanzutti, A., Totis, G., Sortino, M., and Fedrizzi, L., 2020. “Single tracks data obtained by selective laser melting of Ti6Al4V with a small laser spot diameter”. *Data in Brief*, **33**, Dec., p. 106443.
- [57] Kusuma, C., 2016. “The Effect of Laser Power and Scan Speed on Melt Pool Characteristics of Pure Titanium and Ti-6Al-4V Alloy for Selective Laser Melting”. Master’s thesis.

- [58] Dilip, J. J. S., Zhang, S., Teng, C., Zeng, K., Robinson, C., Pal, D., and Stucker, B., 2017. “Influence of processing parameters on the evolution of melt pool, porosity, and microstructures in Ti-6Al-4V alloy parts fabricated by selective laser melting”. *Progress in Additive Manufacturing*, **2**(3), Sept., pp. 157–167.
- [59] Brown, D. A., and Atamturktur, S., 2018. “Nonparametric Functional Calibration of Computer Models”. *Statistica Sinica*, **28**(2), pp. 721–742. Publisher: Institute of Statistical Science, Academia Sinica.
- [60] Pratola, M., Chipman, H., George, E., and McCulloch, R., 2018. Heteroscedastic BART Using Multiplicative Regression Trees, July. arXiv:1709.07542 [stat].
- [61] McCulloch, R., Pratola, M., and Chipman, H., 2019. *rbart: Bayesian Trees for Conditional Mean and Variance*. R package version 1.0.
- [62] Feinberg, J., and Langtangen, H. P., 2015. “Chaospy: An open source tool for designing methods of uncertainty quantification”. *Journal of Computational Science*, **11**, Nov., pp. 46–57.
- [63] Zhang, D., Zhang, P., Liu, Z., Feng, Z., Wang, C., and Guo, Y., 2018. “Thermofluid field of molten pool and its effects during selective laser melting (SLM) of Inconel 718 alloy”. *Additive Manufacturing*, **21**, May, pp. 567–578.
- [64] Nikam, S. H., Quinn, J., and McFadden, S., 2021. “A simplified thermal approximation method to include the effects of marangoni convection in the melt pools of processes that involve moving point heat sources”. *Numerical Heat Transfer, Part A: Applications*, **79**(7), pp. 537–552.
- [65] Lane, B., Zhirnov, I., Mekhontsev, S., Grantham, S., Ricker, R., Rauniyar, S., and Chou, K., 2020. “Transient Laser Energy Absorption, Co-axial Melt Pool Monitoring, and Relationship to Melt Pool Morphology”. *Additive Manufacturing*, **36**, Dec., p. 101504.
- [66] Dilip, J., Anam, M. A., Pal, D., and Stucker, B., 2016. “A short study on the fabrication of single track deposits in SLM and characterization”. In 2016 International Solid Freeform Fabrication Symposium, University of Texas at Austin.
- [67] Liu, B., Fang, G., and Lei, L., 2021. “An analytical model for rapid predicting molten pool geometry of selective laser melting (SLM)”. *Applied Mathematical Modelling*, **92**, Apr., pp. 505–524.

Supplemental Material for
"Probabilistic Printability Maps for Laser Powder Bed Fusion via Functional
Calibration and Uncertainty Propagation"

Nicholas Wu¹, Brendan Whalen², Ji Ma¹, and Prasanna V. Balachandran^{1,2}

¹ Department of Materials Science and Engineering, University of Virginia, Charlottesville, VA 22904

² Department of Mechanical and Aerospace Engineering, University of Virginia, Charlottesville, VA 22904

Submitted to ASME Journal of Computing and Information Science in Engineering
Corresponding author: Prasanna V. Balachandran (pvb5e@virginia.edu)

March 31, 2023

S1 Summary of calibration datasets

S1.1 IN718 calibration data

Lee et al. [8]

Used data from M2 machine for calibration only.

- # of observations: 180
- Powers (W): 120, 180, 240
- Speeds (mm/s): 200, 400, 600, 800, 1000
- Beam diameters (μm): 50, 100, 150
- Layer thicknesses (μm): 25, 50

S1.2 IN625 calibration data

Lee et al. [8]

- # of observations: 176
- Powers (W): 120, 180, 240
- Speeds (mm/s): 200, 400, 600, 800, 1000
- Beam diameters (μm): 50, 100, 150
- Layer thicknesses (μm): 25, 50

S1.3 SS316L calibration data

Bertoli et al., [11] Goosens et al., [3] Hu et al., [4]

- # of observations: 113
- Power (W): 40, 50, 60, 70, 80, 90, 100, 150, 200, 300, 400, 500, 600
- Speeds (mm/s): 150, 200, 250, 300, 400, 450, 500, 600, 700, 750, 800, 900, 1000, 1100, 1200, 1250, 1500, 1800, 2000
- Beam diameters (μm): 15, 37.5, 52, 55
- Layer thicknesses (μm): 10, 30, 50, 75

S1.4 Ti6Al4V calibration data

Kusuma [6], Vaglio et al. [12], Dilip et al. [2], Patel et al. [10]

- # of observations: 128
- Powers (W): 50, 90, 100, 120, 130, 150, 160, 170, 190, 200, 210, 220, 250, 260, 300, 350, 400
- Speeds (mm/s): 200, 250, 500, 730, 750, 800, 850, 870, 1000, 1100, 1150, 1200, 1250, 1360, 1500, 1750, 2000, 2250, 2500
- Beam diameters (μm): 50, 70, 100
- Layer thicknesses (μm): 25, 30, 70

S2 Including beam diameter as a feature in the HBART model does not improve fit on geometry prediction

To evaluate whether including beam diameter in the HBART model improved predictive performance, we fitted two sets of models to the parameter samples obtained from Bayesian calibration, one with and one without. In the set with beam diameter, we included the average beam diameter as a feature for HBART (see the main body of the paper, Section 2.3). For the analyses conducted in the main body of the paper, we do not use the beam diameter as a feature to HBART. We use both models to predict the effective absorptivity and effective porosity, then propagate these parameters through the modified ET model using polynomial chaos and evaluate the fit on the calibration data set as in Section 3.2 of the main body of the paper. We primarily consider the fit on the melt pool depth data, as both models performed well for the melt pool width.

Figures S-1, S-2, S-3, S-4 illustrate that including beam diameter as a feature fails to resolve any systematic discrepancy between experiment and prediction. In addition, including beam diameter sometimes decreased R^2 (as in the case of IN625, IN718), and sometimes increased R^2 (for SS316L, Ti6Al4V). Overall, since including beam diameter did not improve the fit of the model, we did not include it as a feature for HBART.

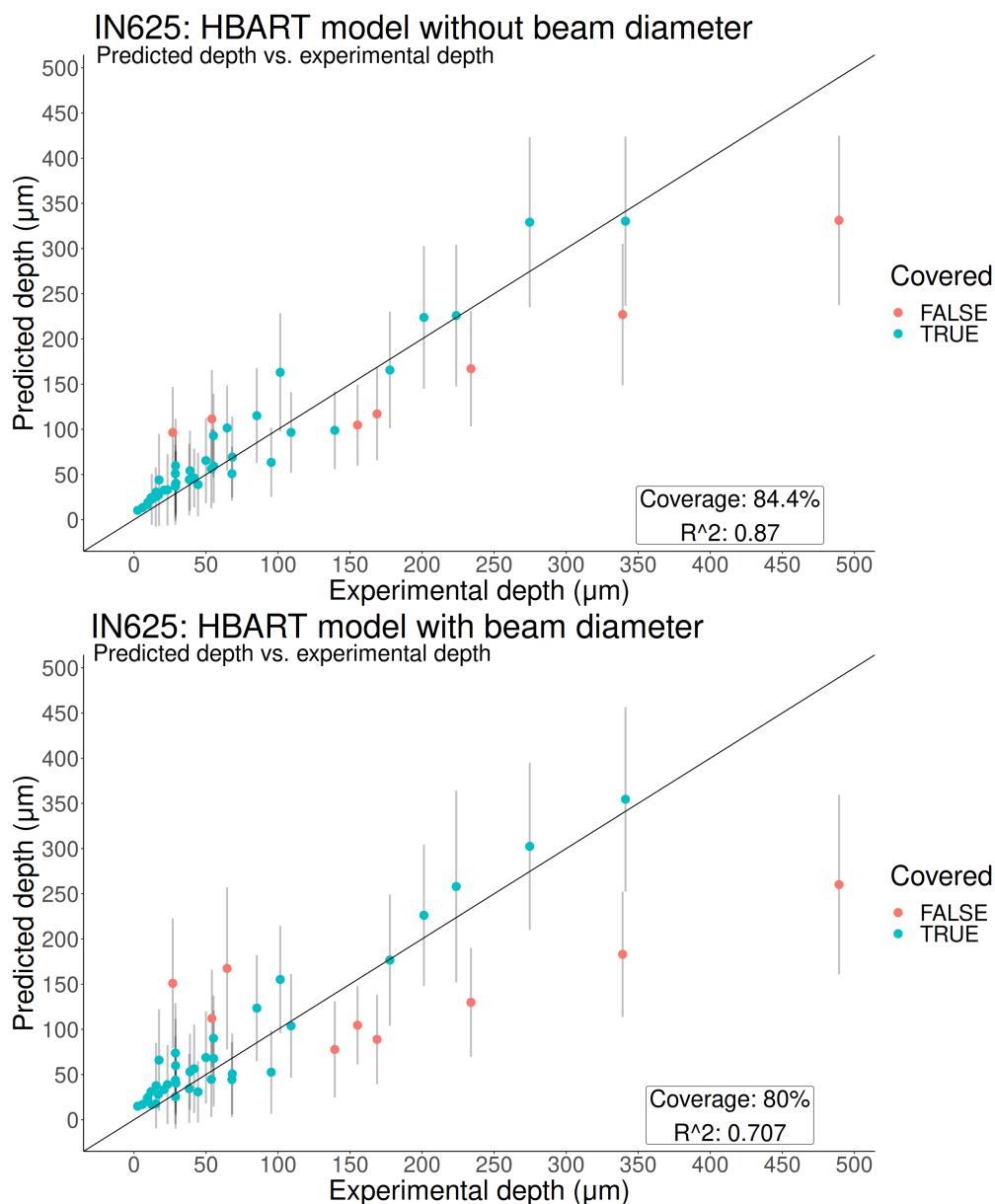


Figure S-1: Comparison of predicted depth and experimental depth for IN625. The top figure shows the prediction using the HBART model without beam diameter as a feature. The lower figure shows the prediction using the HBART model with beam diameter as a feature. Including beam diameter decreases the R^2 of the model and does not significantly affect the qualitative properties of the fit.

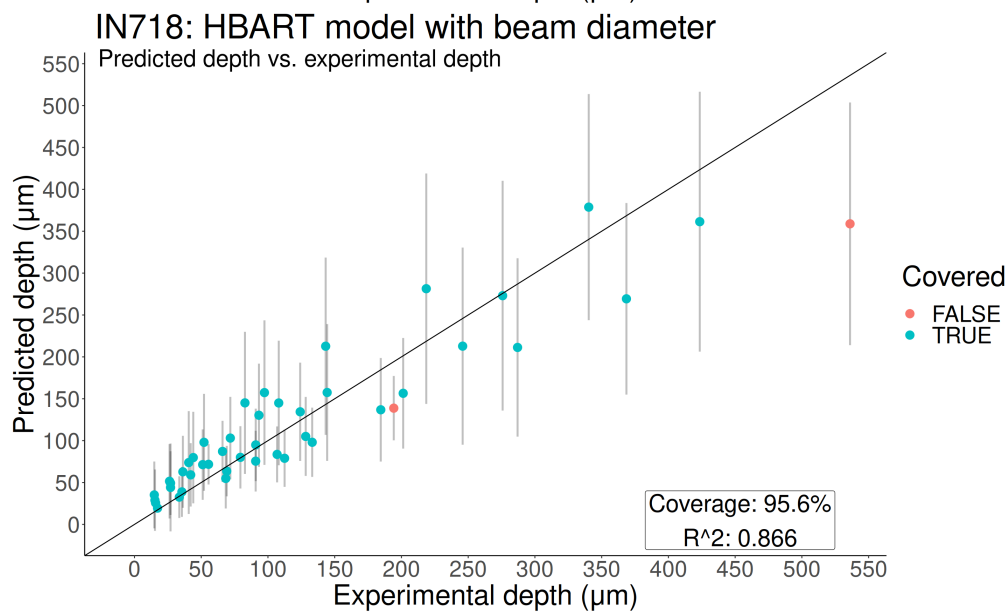
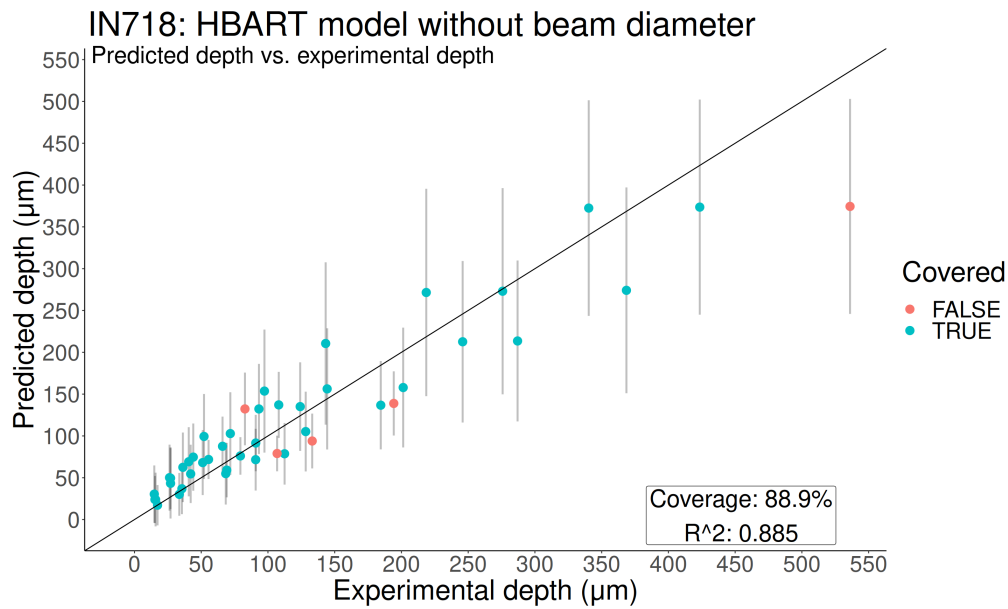


Figure S-2: Comparison of predicted depth and experimental depth for IN718. The top figure shows the prediction using the HBART model without beam diameter as a feature. The lower figure shows the prediction using the HBART model with beam diameter as a feature. Including beam diameter decreases the R^2 of the model and does not significantly affect the qualitative properties of the fit.

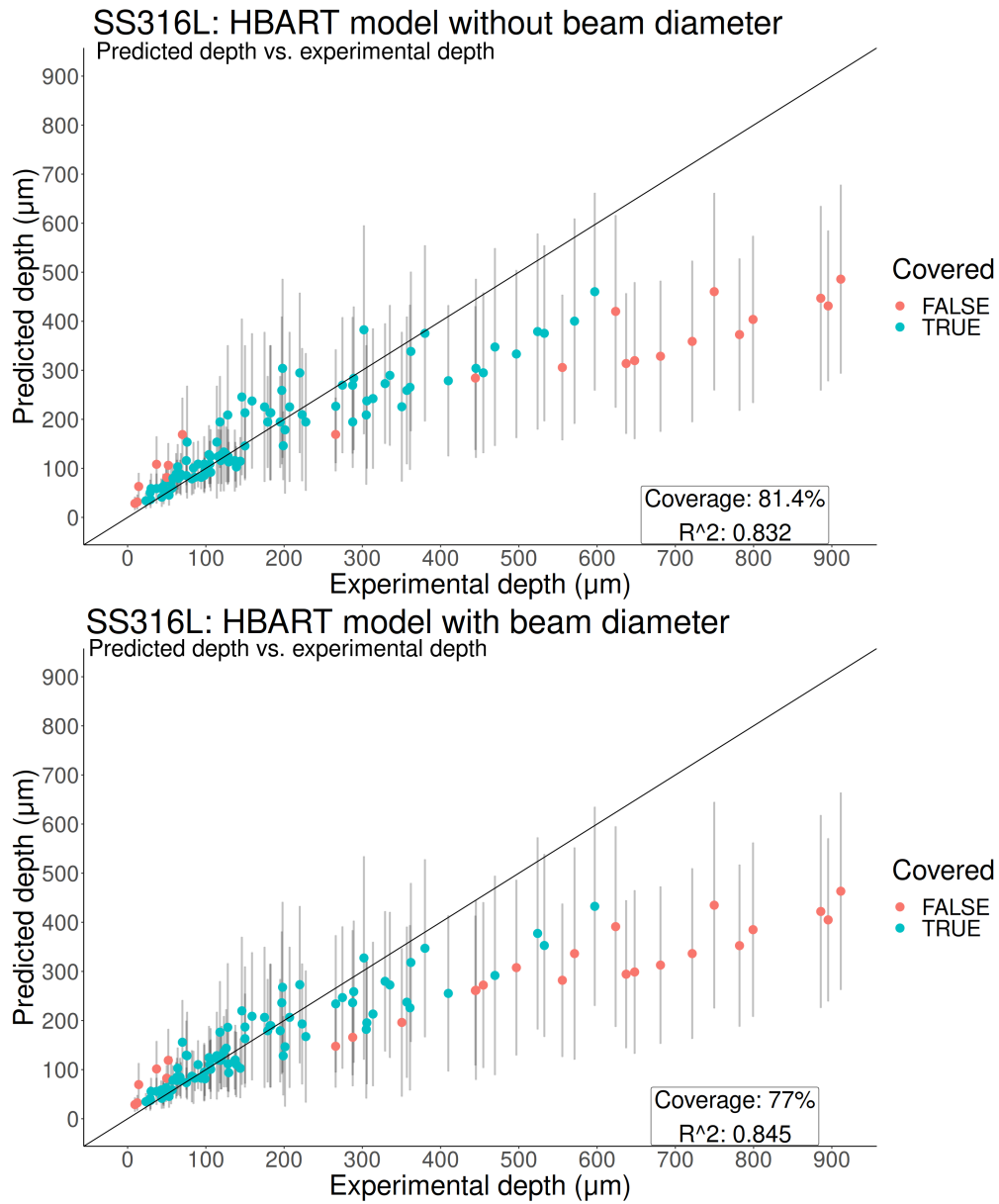


Figure S-3: Comparison of predicted depth and experimental depth for SS316L. The top figure shows the prediction using the HBART model without beam diameter as a feature. The lower figure shows the prediction using the HBART model with beam diameter as a feature. Including beam diameter increases the R^2 of the model, but does not significantly affect the qualitative properties of the fit.

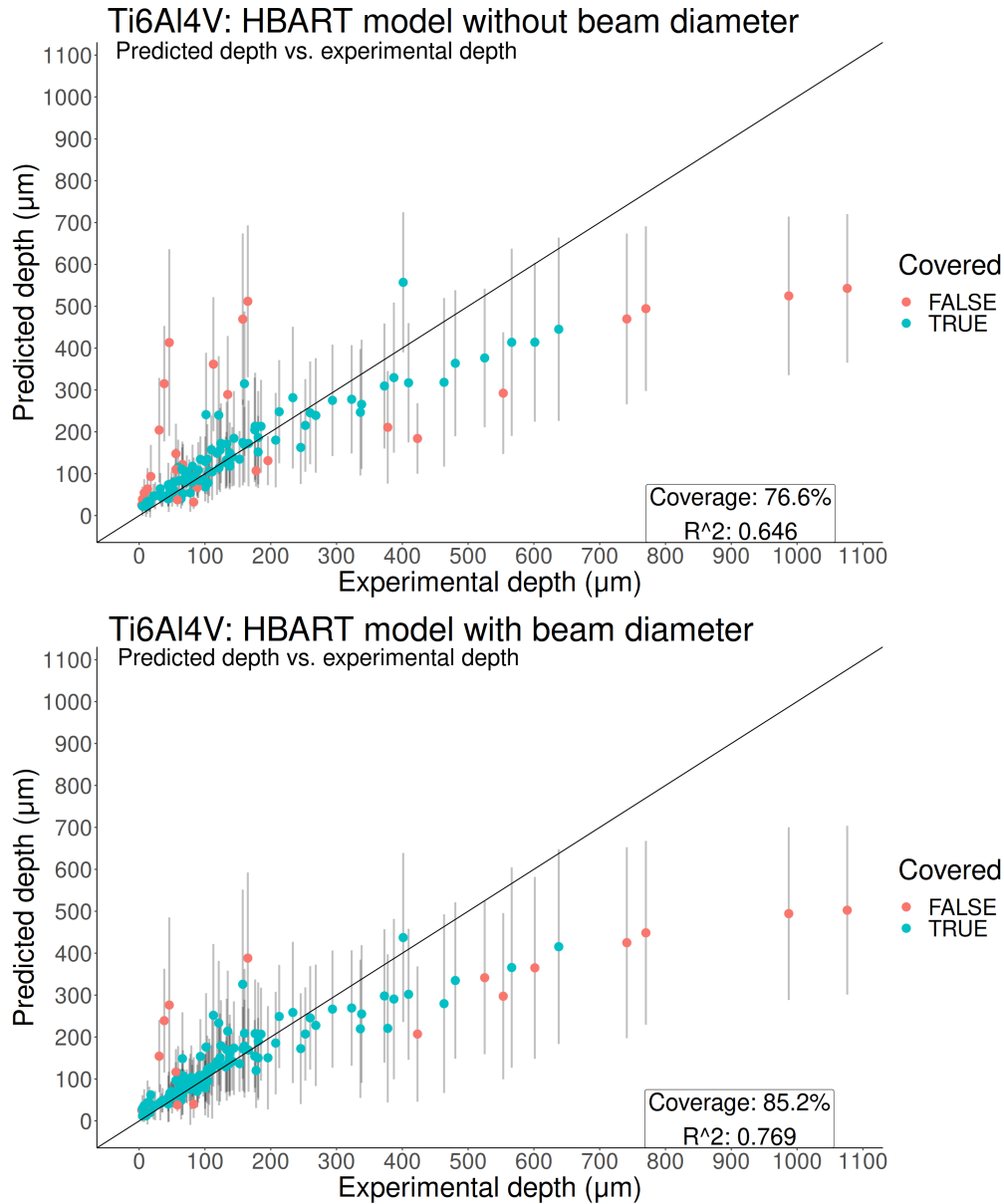


Figure S-4: Comparison of predicted depth and experimental depth for Ti6Al4V. The top figure shows the prediction using the HBART model without beam diameter as a feature. The lower figure shows the prediction using the HBART model with beam diameter as a feature. Including beam diameter increases the R^2 of the model, but does not significantly affect the qualitative properties of the fit.

S3 Monte Carlo uncertainty propagation yields an approximately normal distribution

To assess whether it was valid to model the depth as a normal distribution, we carried out Monte-Carlo uncertainty propagation. We considered this for the case of IN718. After calibration, we obtained normal posterior distributions for absorptivity and porosity, then sampled from these posterior distributions to perform Monte-Carlo uncertainty propagation. We assessed the distributions for the power and speed combinations present in the Lee et al. dataset. We drew 700 samples for each parameter combination. It can be observed that the distribution of predicted depth does not deviate significantly from the normal fit. (Figures S-5, S-6, S-7)

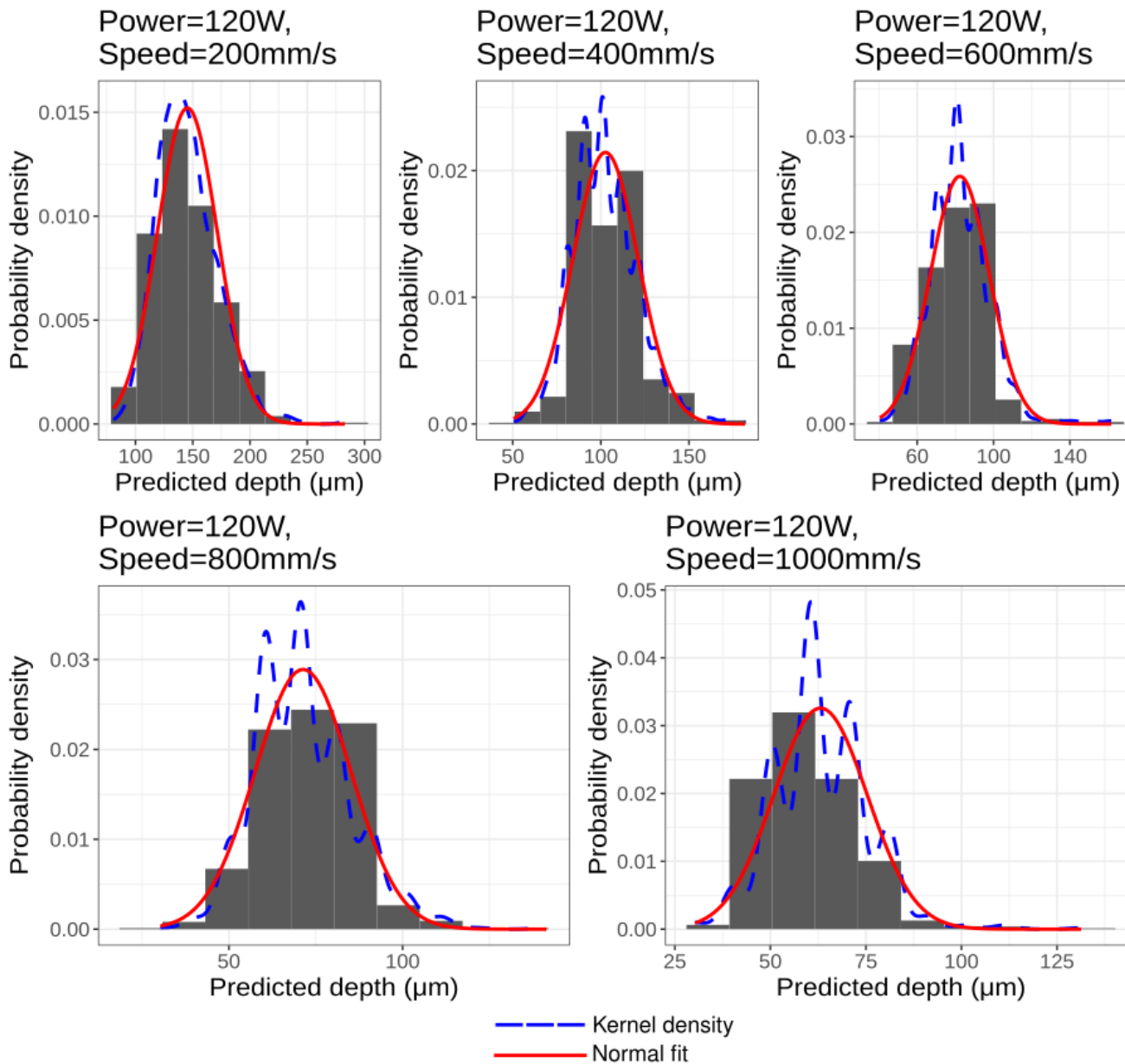


Figure S-5: Histograms of predicted melt pool depth obtained by Monte-Carlo uncertainty propagation, where the power is fixed at 120 W. Speeds increase from left to right and top to bottom, ranging from 200 mm/s to 1000 mm/s. A kernel density estimate is plotted over the histogram in blue. The normal fit (calculated from the sample mean and SD) is plotted over in samples in red. The kernel density estimate does not strongly deviate from the normal fit.

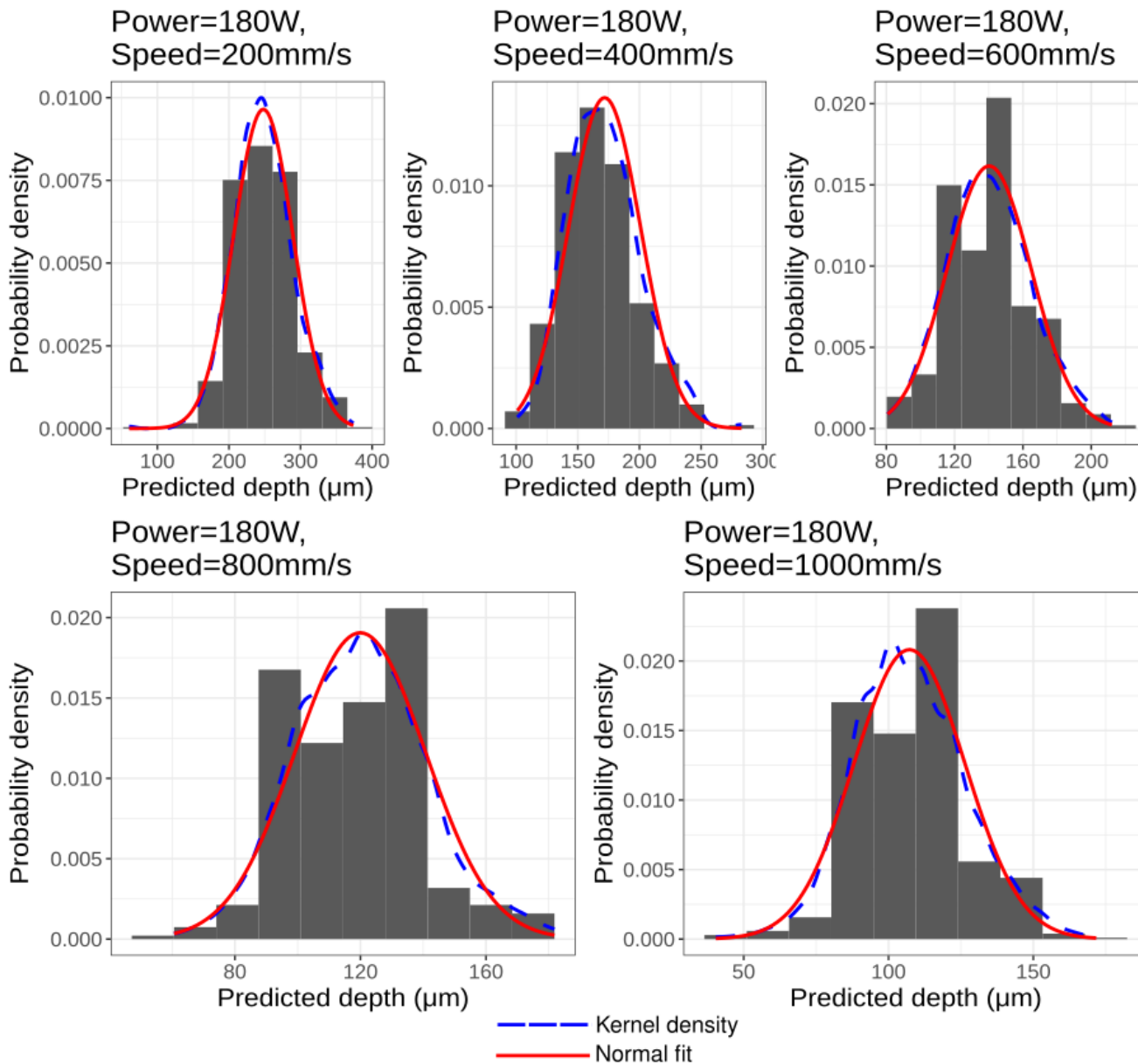


Figure S-6: Histograms of predicted melt pool depth obtained by Monte-Carlo uncertainty propagation, where the power is fixed at 180 W. Speeds increase from left to right and top to bottom, ranging from 200 mm/s to 1000 mm/s. A kernel density estimate is plotted over the histogram in blue. The normal fit (calculated from the sample mean and SD) is plotted over in samples in red. The kernel density estimate does not strongly deviate from the normal fit.

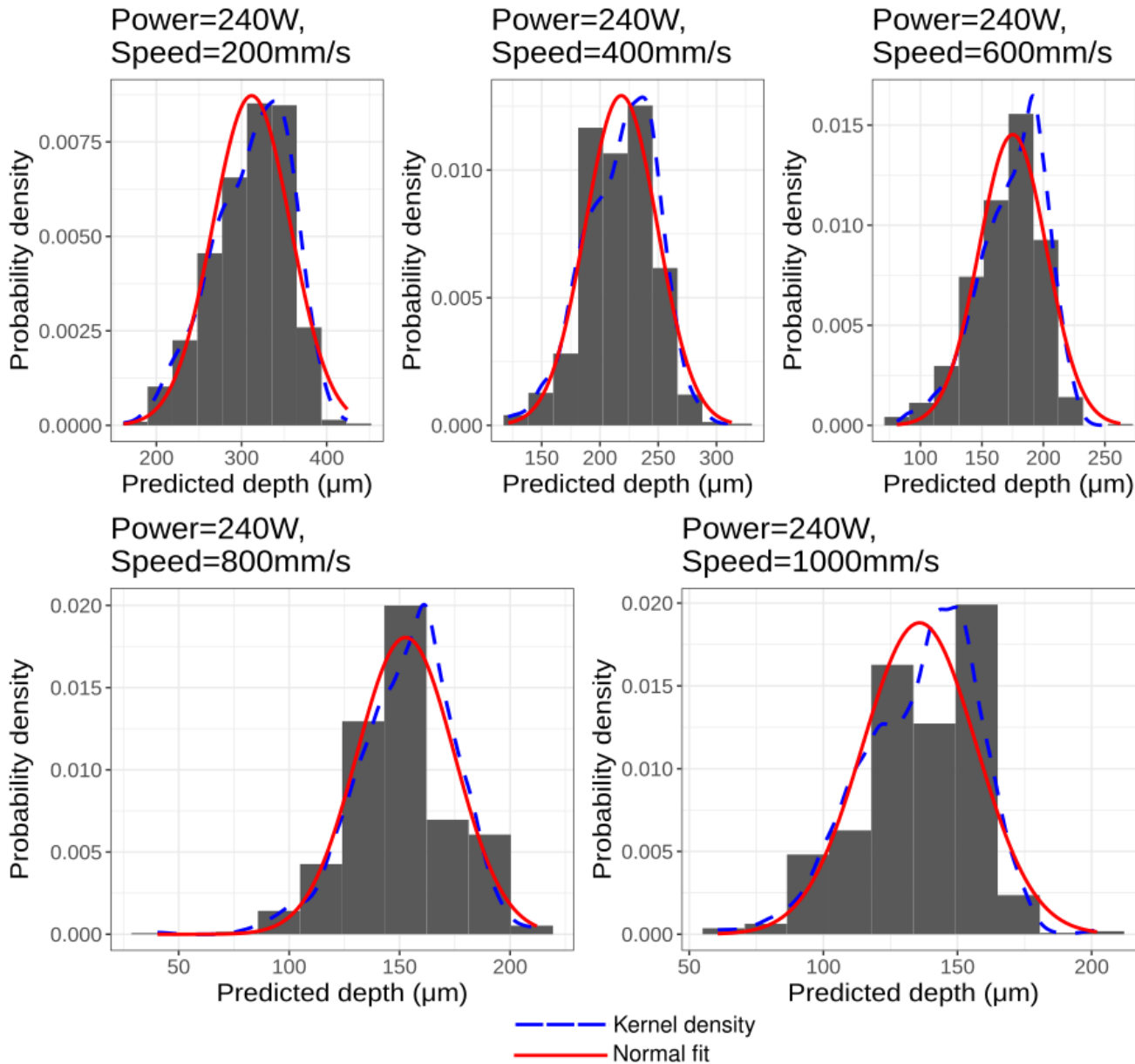


Figure S-7: Histograms of predicted melt pool depth obtained by Monte-Carlo uncertainty propagation, where the power is fixed at 240 W. Speeds increase from left to right and top to bottom, ranging from 200 mm/s to 1000 mm/s. A kernel density estimate is plotted over the histogram in blue. The normal fit (calculated from the sample mean and SD) is plotted over in samples in red. The kernel density estimate does not strongly deviate from the normal fit.

S4 Modified ET Model melt pool predictions without calibration

This section provides unfitted predictions for all materials considered in this work. The details for producing these results is in Section 3.1 of the main paper. All plots exhibit the same trend of underpredicted depth and overpredicted width.

S4.1 IN625

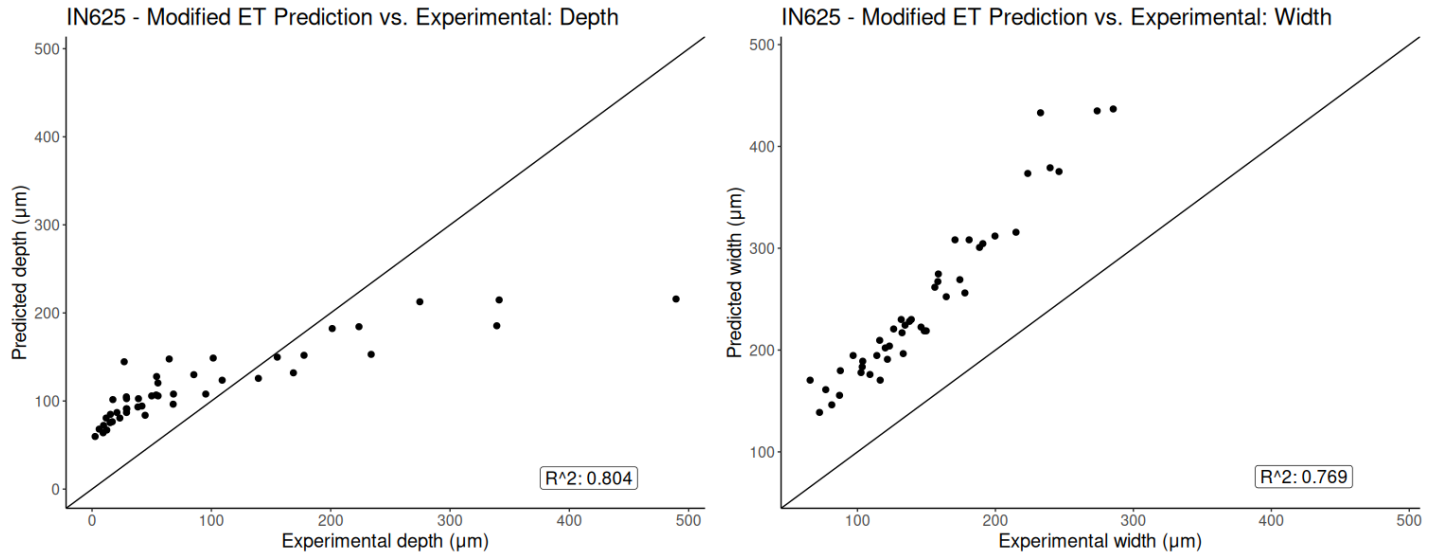


Figure S-8: IN625 predicted melt pool geometry vs. experimental melt pool geometry. The left plot shows the comparison of predicted melt pool depth against experimental melt pool depth. The right plot shows the comparison of predicted melt pool width against experimental melt pool width.

S4.2 IN718

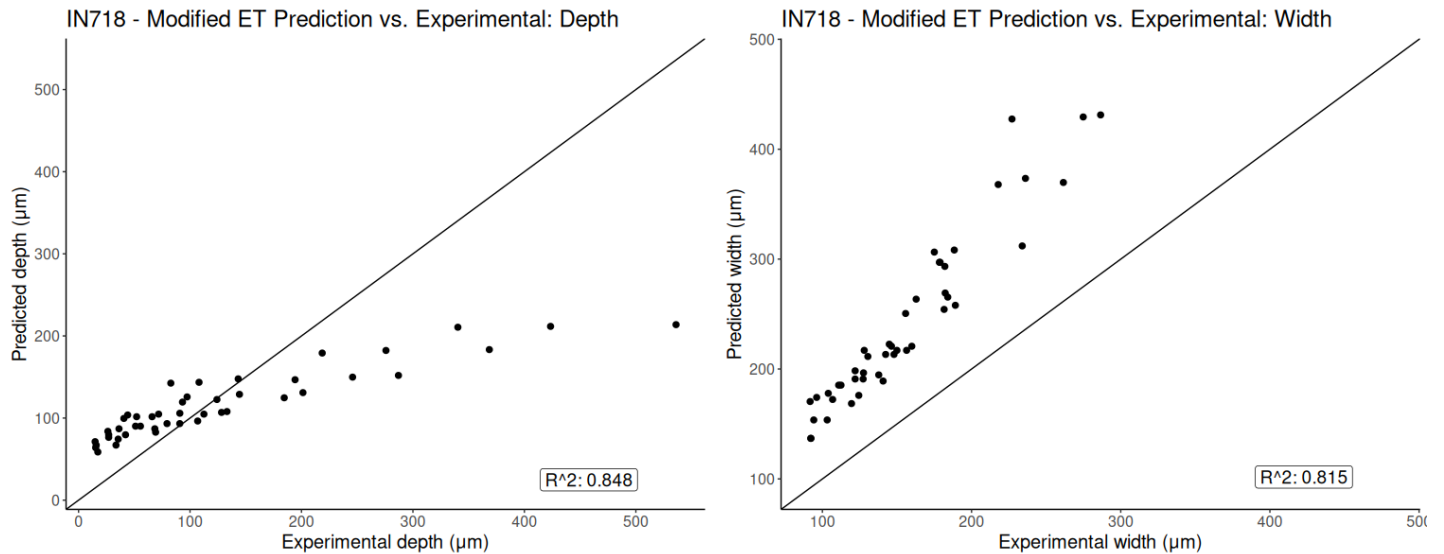


Figure S-9: IN718 predicted melt pool geometry vs. experimental melt pool geometry. The left plot shows the comparison of predicted melt pool depth against experimental melt pool depth. The right plot shows the comparison of predicted melt pool width against experimental melt pool width.

S4.3 SS316L

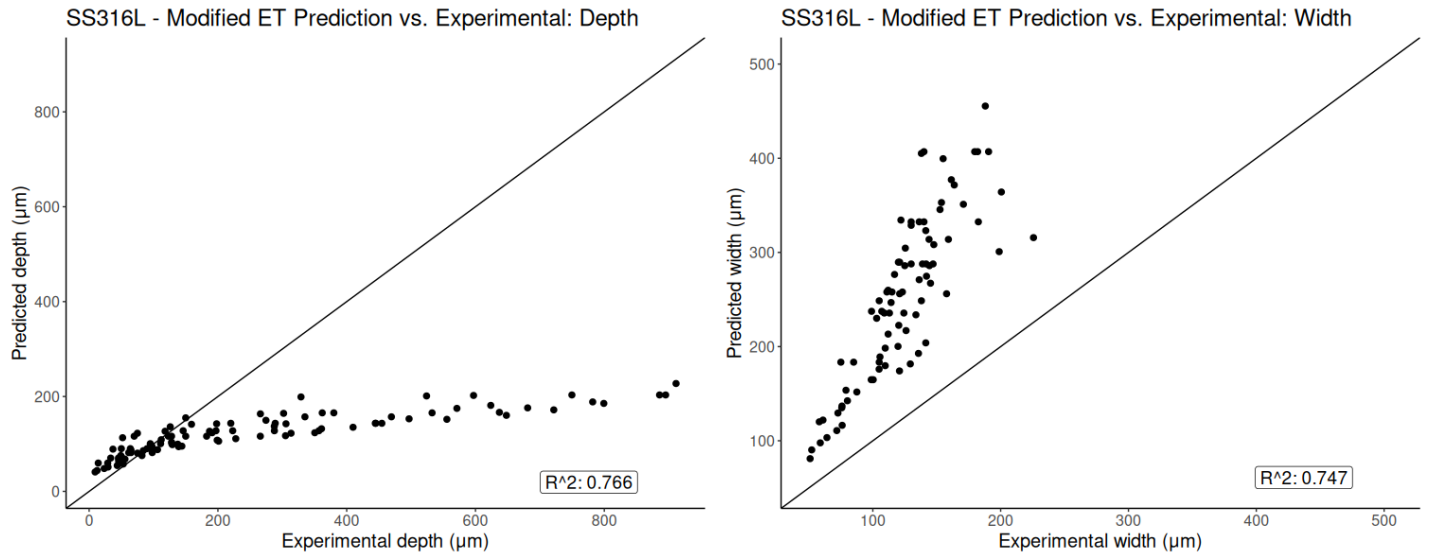


Figure S-10: SS316L predicted melt pool geometry vs. experimental melt pool geometry. The left plot shows the comparison of predicted melt pool depth against experimental melt pool depth. The right plot shows the comparison of predicted melt pool width against experimental melt pool width.

S4.4 Ti6Al4V unfitted predictions

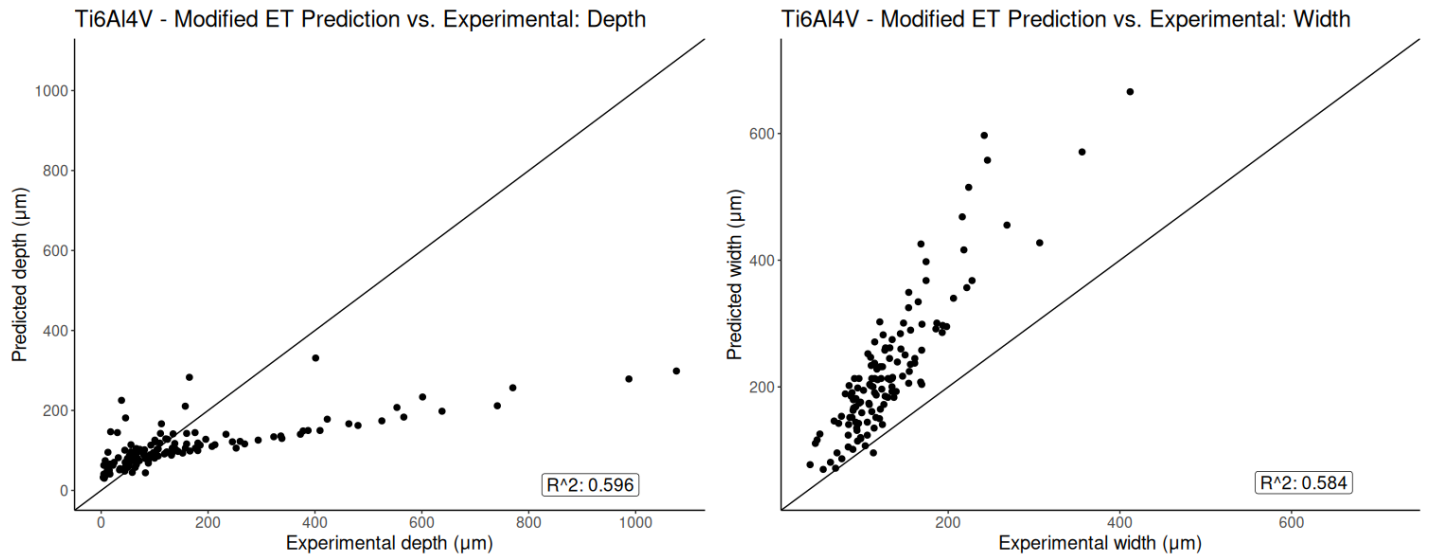


Figure S-11: Ti6Al4V predicted melt pool geometry vs. experimental melt pool geometry. The left plot shows the comparison of predicted melt pool depth against experimental melt pool depth. The right plot shows the comparison of predicted melt pool width against experimental melt pool width.

S5 Absorptivity and porosity curves

Here, representative curves of the fitted effective absorptivity and effective porosity are plotted. See Section 2.3 and Section 3.2 of the main paper for more information.

S5.1 IN718

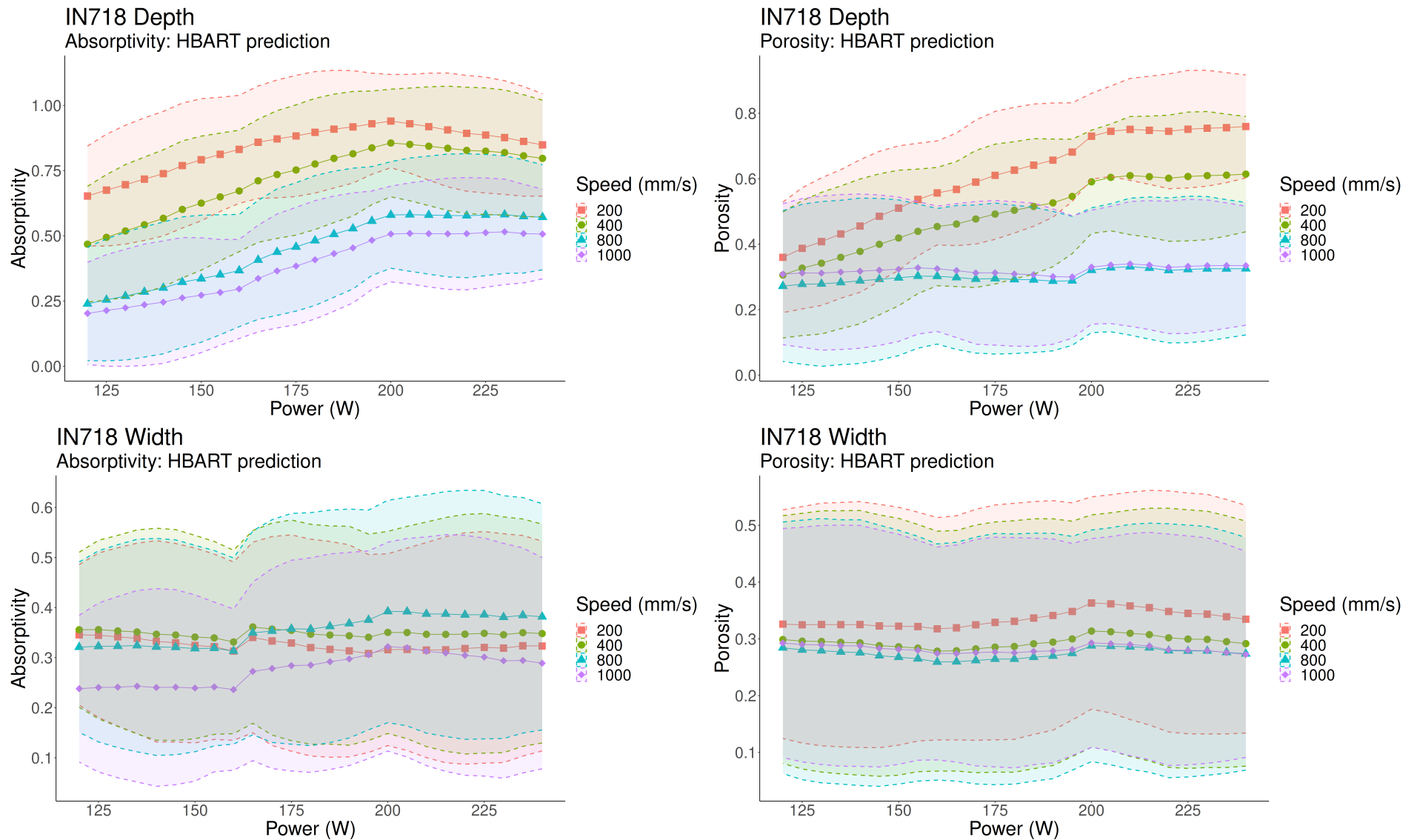


Figure S-12: Plots of effective absorptivity and effective porosity for IN718. The top left plot shows the depth-fitted absorptivity η_d . The top right plot shows the depth-fitted porosity ϕ_d . The bottom left plot shows the width-fitted absorptivity η_w . The bottom right plot shows the width-fit porosity ϕ_w . η_d and ϕ_d increase with respect to power and decrease with respect to speed. In contrast, η_w and ϕ_w are practically constant with respect to both power and speed.

S5.2 IN625

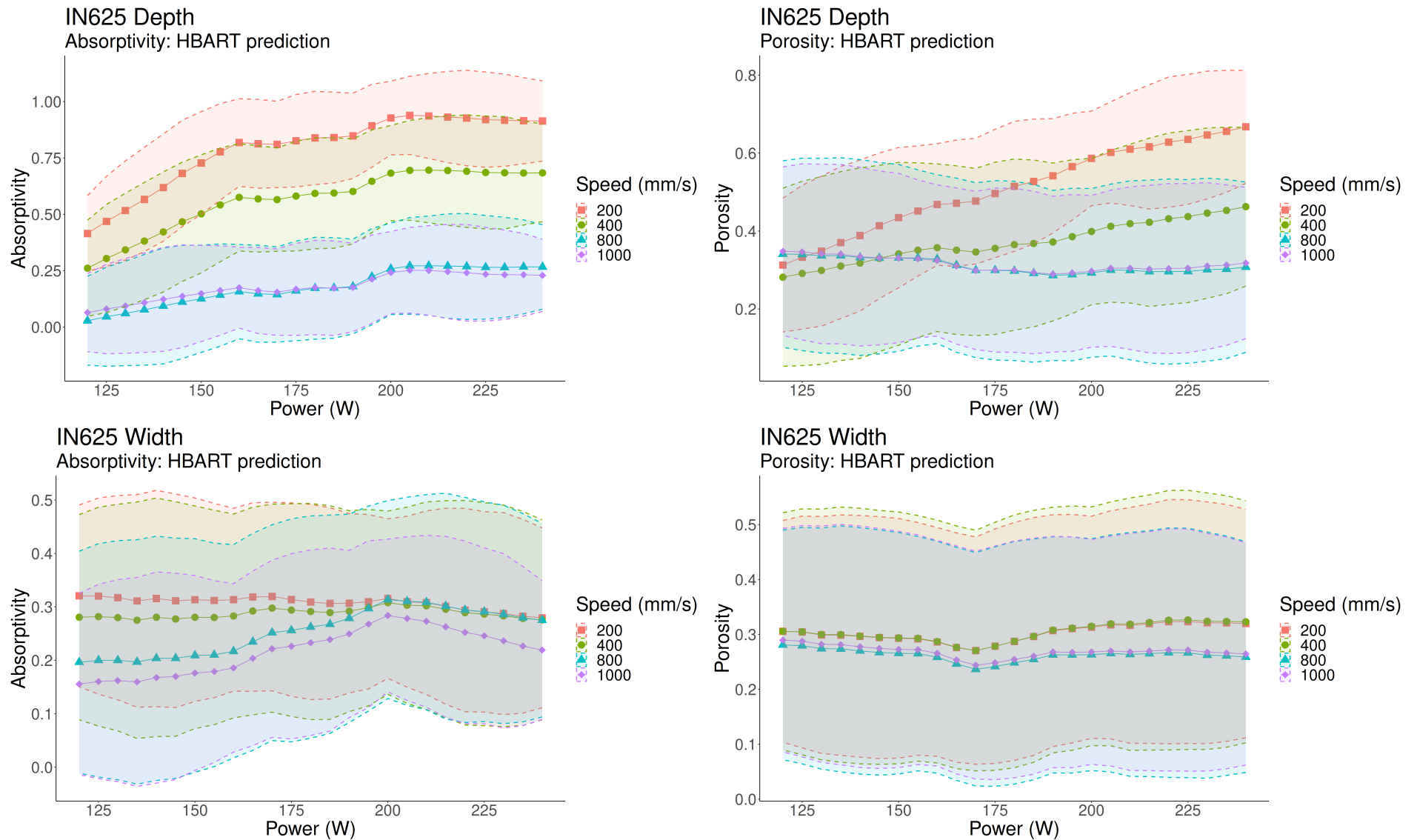


Figure S-13: Plots of effective absorptivity and effective porosity for IN625. The top left plot shows the depth-fitted absorptivity η_d . The top right plot shows the depth-fitted porosity ϕ_d . The bottom left plot shows the width-fitted absorptivity η_w . The bottom right plot shows the width-fit porosity ϕ_w . η_d and ϕ_d increase with respect to power and decrease with respect to speed. In contrast, η_w and ϕ_w are practically constant with respect to both power and speed.

S5.3 SS316L

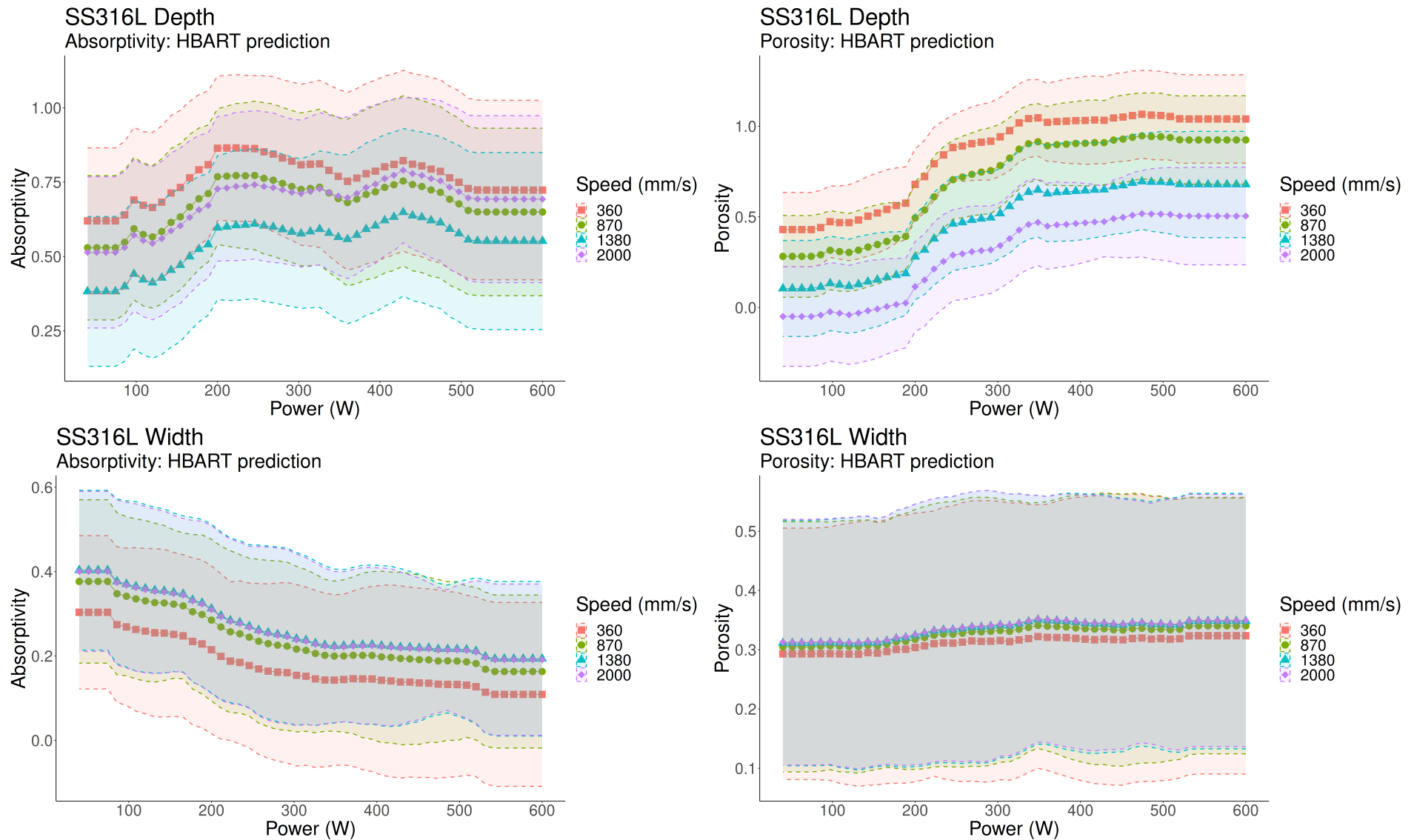


Figure S-14: Plots of effective absorptivity and effective porosity for SS316L. The top left plot shows the depth-fitted absorptivity η_d . The top right plot shows the depth-fitted porosity ϕ_d . The bottom left plot shows the width-fitted absorptivity η_w . The bottom right plot shows the width-fit porosity ϕ_w . ϕ_d increases with respect to power and decreases with respect to speed. η_d exhibits a jagged, non-monotonic trend with respect to power and speed. However, this is difficult to interpret due to the large uncertainty. ϕ_w is practically constant with respect to both power and speed. However, η_w appears to decrease with respect to power, but not as significantly with respect to speed.

S5.4 Ti6Al4V

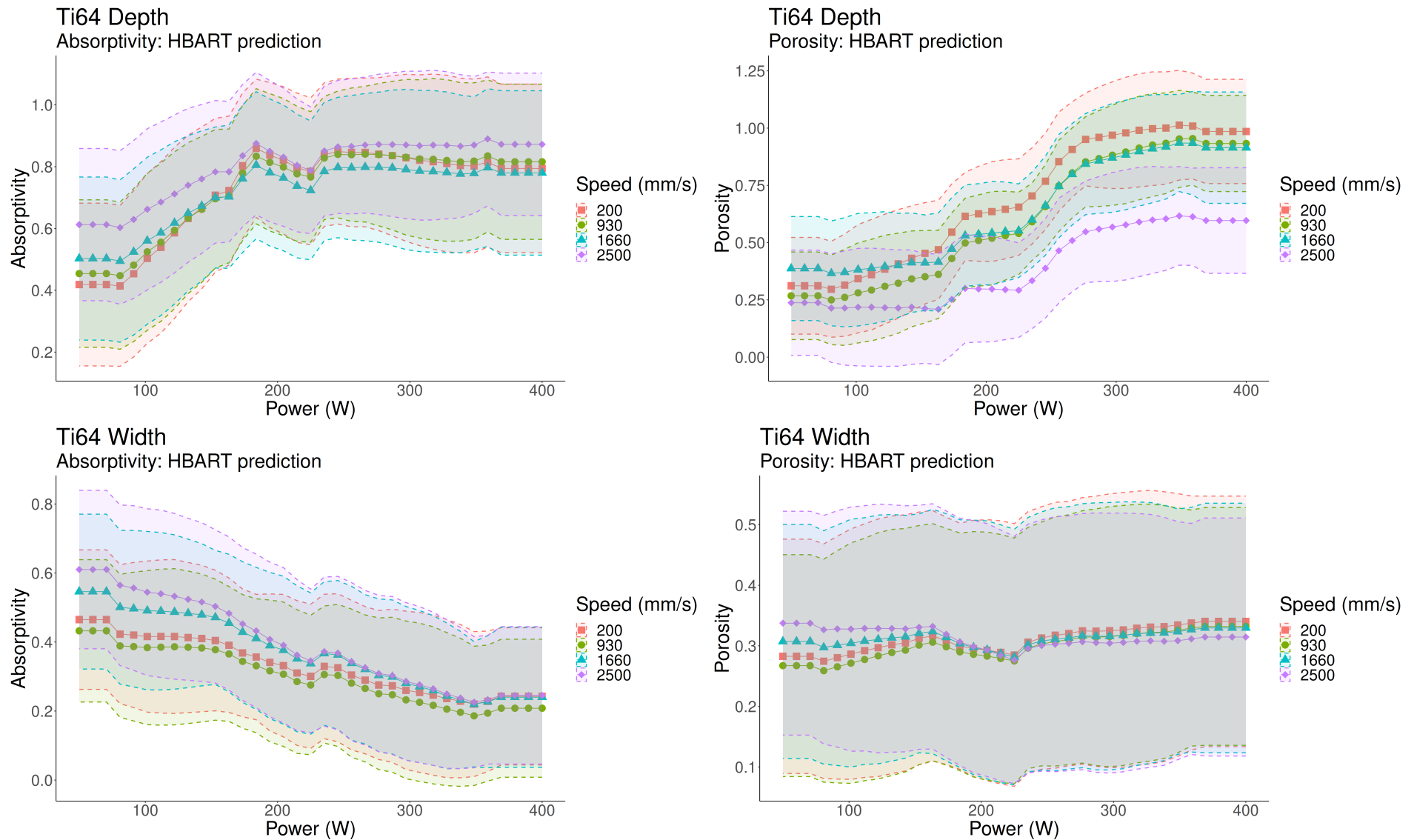


Figure S-15: Plots of effective absorptivity and effective porosity for Ti6Al4V. The top left plot shows the depth-fitted absorptivity η_d . The top right plot shows the depth-fitted porosity ϕ_d . The bottom left plot shows the width-fitted absorptivity η_w . The bottom right plot shows the width-fit porosity ϕ_w . ϕ_d and η_d increase with respect to power and decrease with respect to speed. ϕ_w is practically constant with respect to both power and speed. However, η_w appears to decrease with respect to power, but not as significantly with respect to speed.

S6 Uncertainty propagation: width and depth

This section shows the plots for calculations to assess in-sample fit, corresponding to Section 3.3 in the main paper. The results of these calculations are summarized in Table 5 in the main paper.

S6.1 IN718

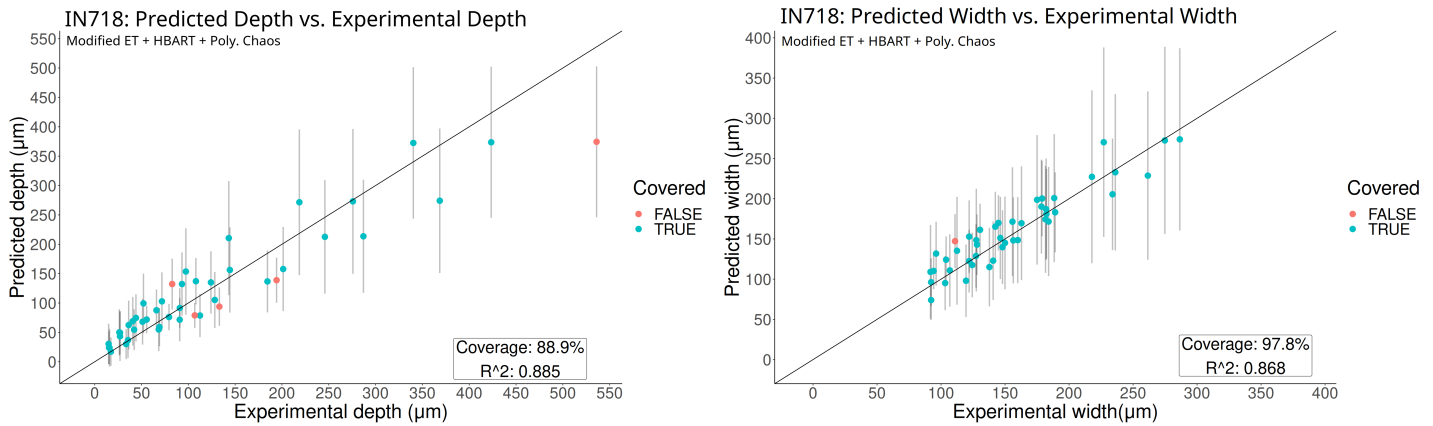


Figure S-16: In-sample predictions for IN718, comparing predicted melt pool geometry with experimental melt pool geometry from calibration data. The left plot shows the predicted depth vs. the experimental depth. The right plot shows the predicted width vs. the experimental width.

S6.2 IN625

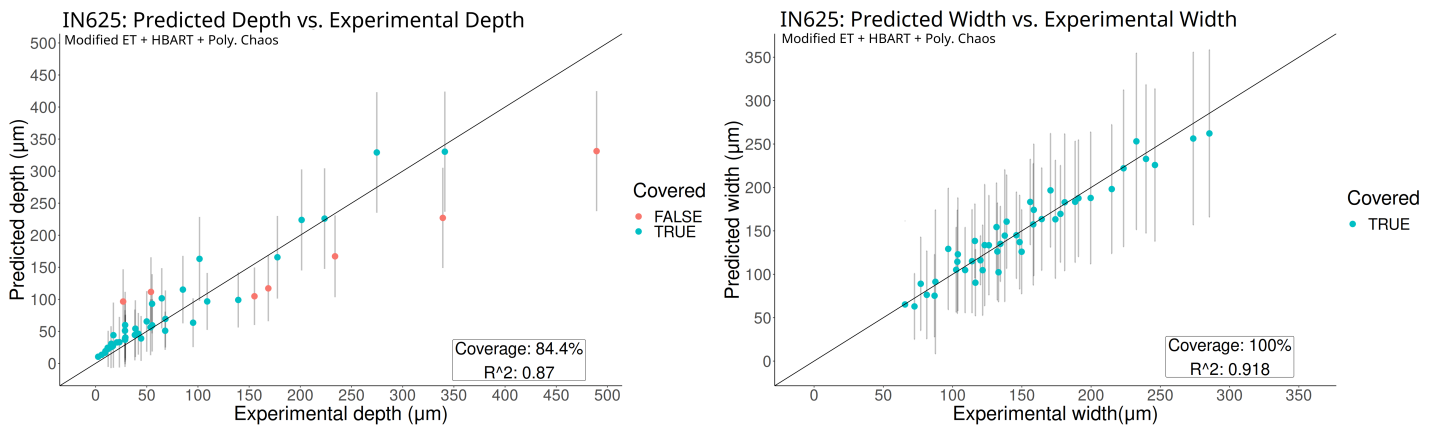


Figure S-17: In-sample predictions for IN625, comparing predicted melt pool geometry with experimental melt pool geometry from calibration data. The left plot shows the predicted depth vs. the experimental depth. The right plot shows the predicted width vs. the experimental width.

S6.3 SS316L

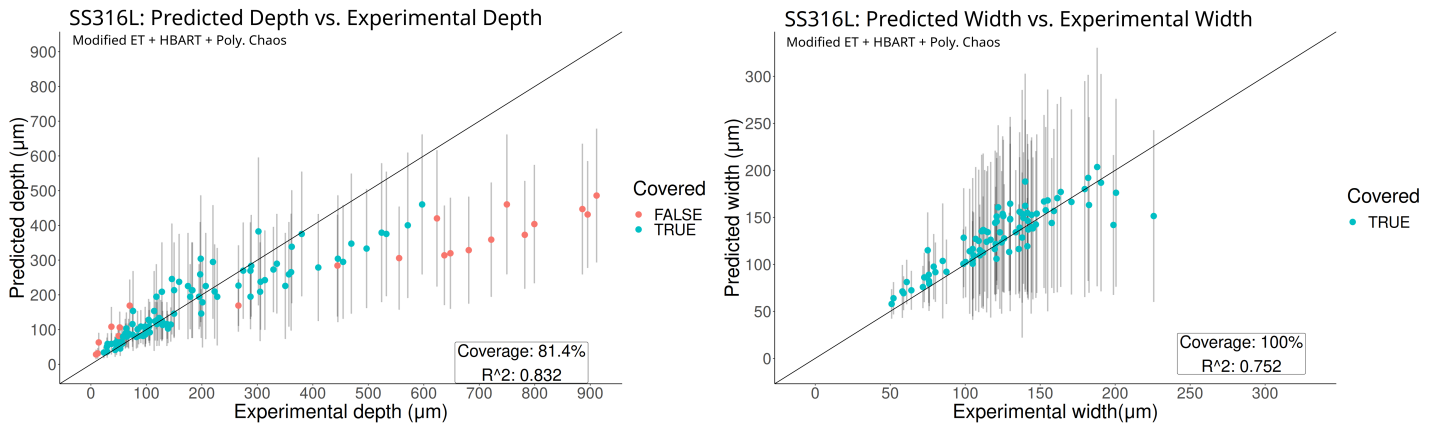


Figure S-18: In-sample predictions for SS316L, comparing predicted melt pool geometry with experimental melt pool geometry from calibration data. The left plot shows the predicted depth vs. the experimental depth. The right plot shows the predicted width vs. the experimental width.

S6.4 Ti6Al4V

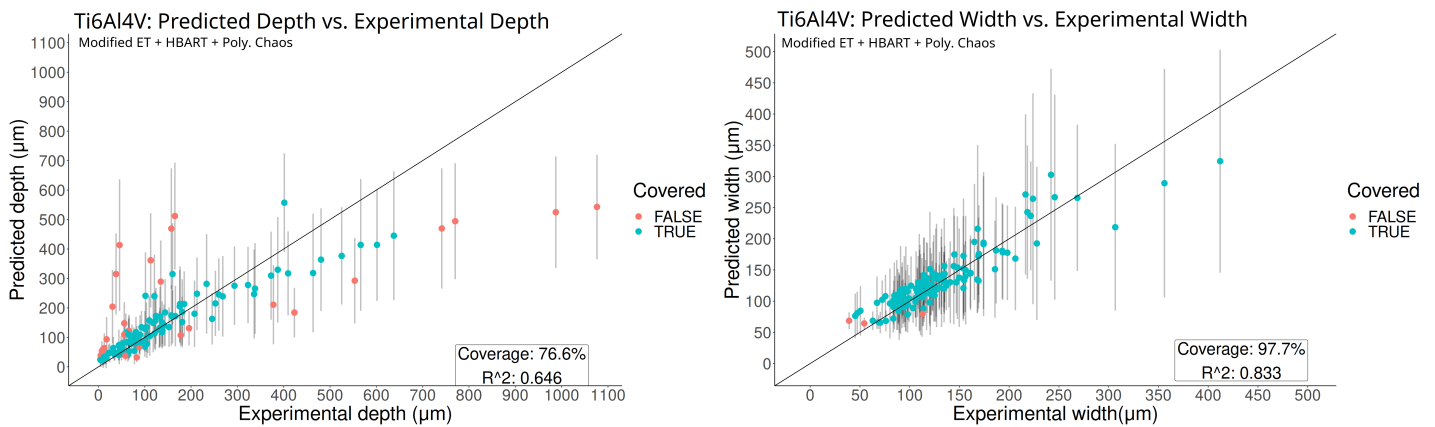


Figure S-19: In-sample predictions for Ti6Al4V, comparing predicted melt pool geometry with experimental melt pool geometry from calibration data. The left plot shows the predicted depth vs. the experimental depth. The right plot shows the predicted width vs. the experimental width.

S7 Model validation by out-of-sample geometry prediction

This section shows plots for out-of-sample prediction, corresponding to Section 3.3 in the main paper. The results of these calculations are summarized in Table 6 in the main paper.

S7.1 Summary of validation data

IN625: Dilip et al. [1]

- # of observations: 33
- Powers (W): 50, 75, 100, 125, 150, 175, 195
- Speeds (mm/s): 200, 400, 600, 800, 1000, 1200
- Beam diameters (μm): 100
- Layer thicknesses (μm): 20

IN625: Lane et al. [7]

- # of observations: 9
- Powers (W): 50, 65, 80, 100, 120, 150, 200, 250, 300
- Speeds (mm/s): 500
- Beam diameters (μm): 62
- Layer thicknesses (μm): 60

IN718: Lee et al. (Mlab data) [8]

- # of observations: 117
- Powers (W): 70, 80, 90, 100
- Speeds (mm/s): 500, 700, 800, 900, 1100
- Beam diameters (μm): 50
- Layer thicknesses (μm): 25, 35, 45

Ti6Al4V: Liu et al. [9]

- # of observations: 26
- Powers (W): 50, 100, 150, 200, 250, 300, 350
- Speeds (mm/s): 200, 240, 320, 400, 480, 560, 600, 800, 1000, 1200, 1400, 1600, 2000
- Beam diameters (μm): 100
- Layer thicknesses (μm): 0 (bare plate), 30, 60

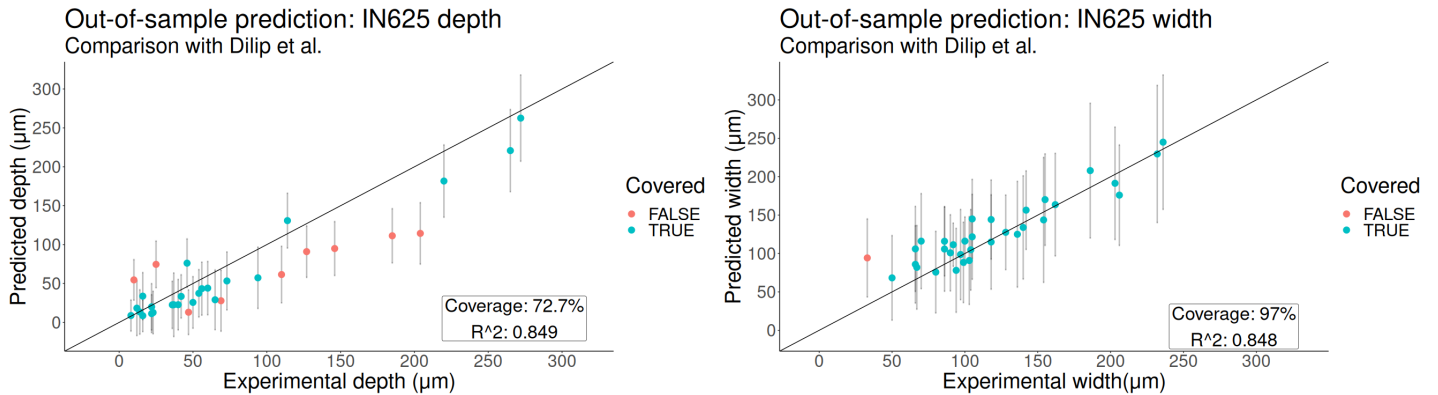


Figure S-20: Predicted melt pool geometry vs. experimental melt pool geometry from Dilip et al. [1]. Overall, the model performs well on this dataset. The depth uncertainty is somewhat under-quantified.

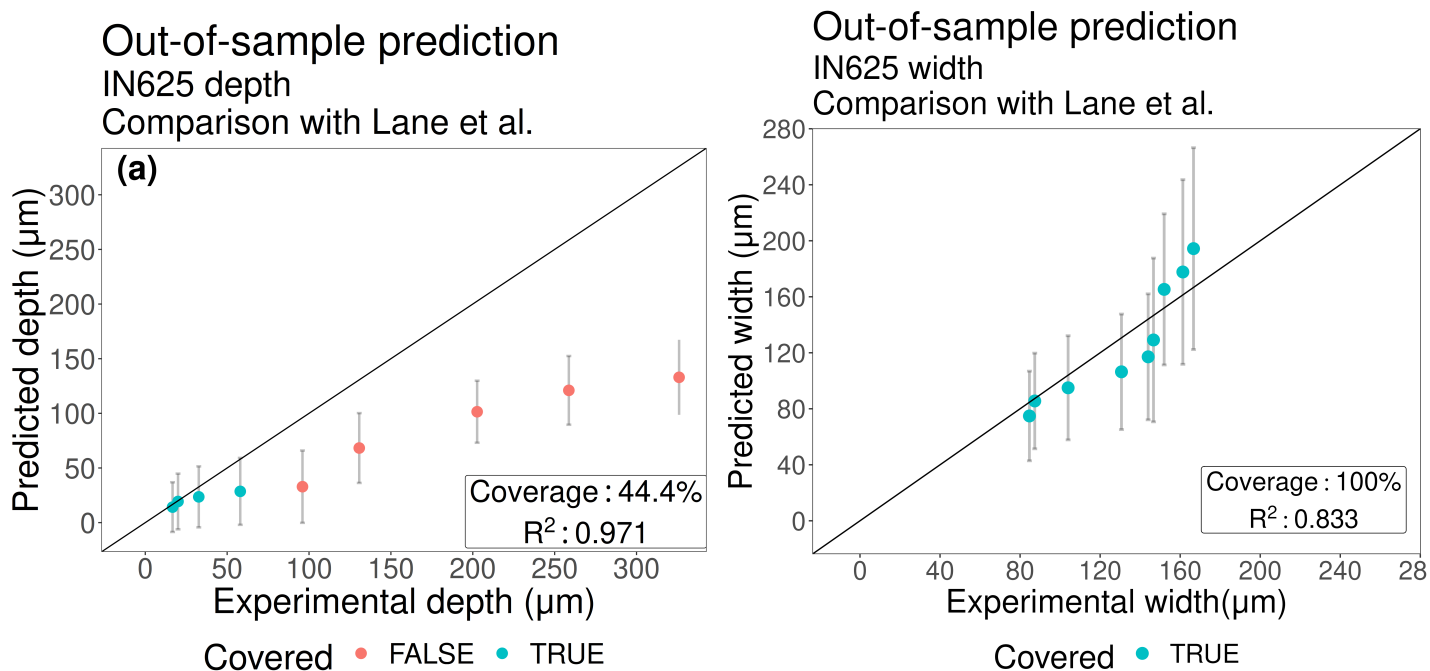


Figure S-21: Predicted melt pool geometry vs. experimental melt pool geometry from Lane et al. [7]. There is a systematic discrepancy between experiment and prediction for the case of the melt pool depth. However, the width predictions show reasonable agreement and fall within the error bars.

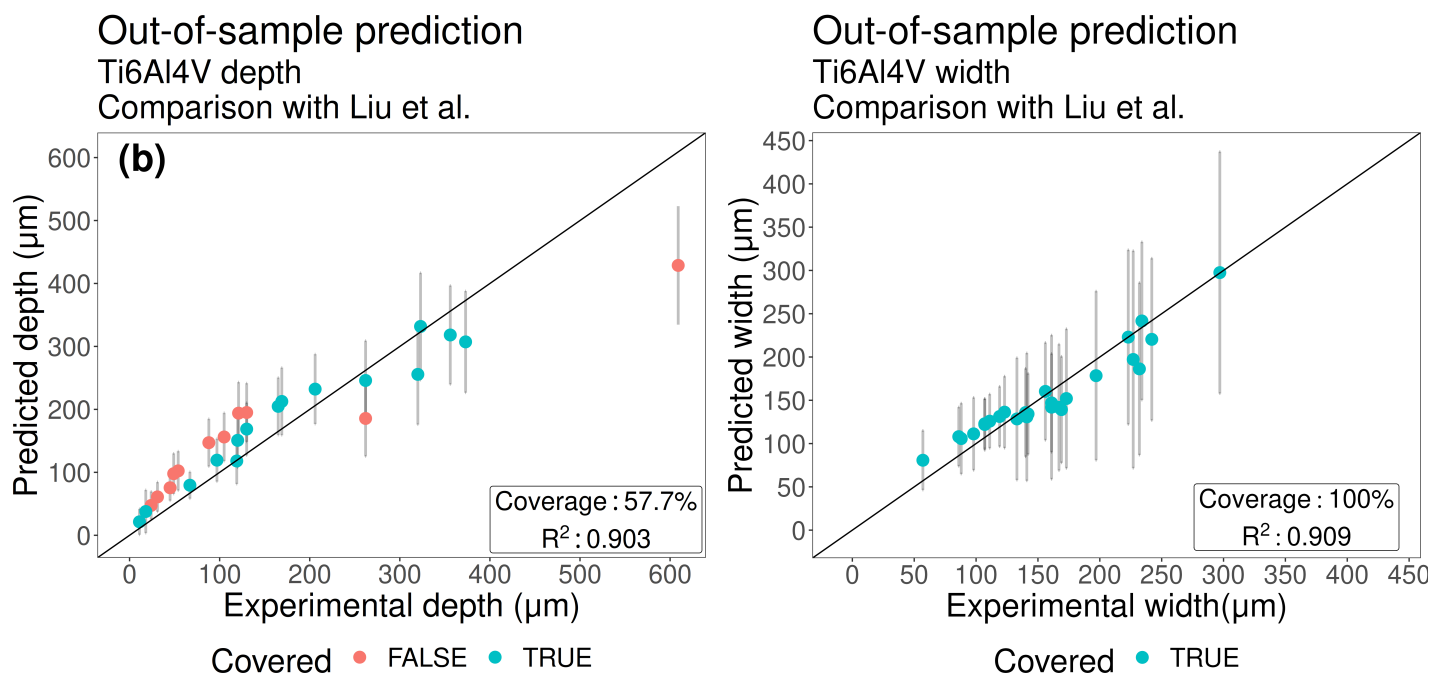


Figure S-22: Predicted melt pool geometry vs. experimental melt pool geometry from Liu et al. [9]. Overall, the model seems to perform well on this dataset. The depth uncertainty is somewhat under-quantified. An observation with high depth is under-predicted.

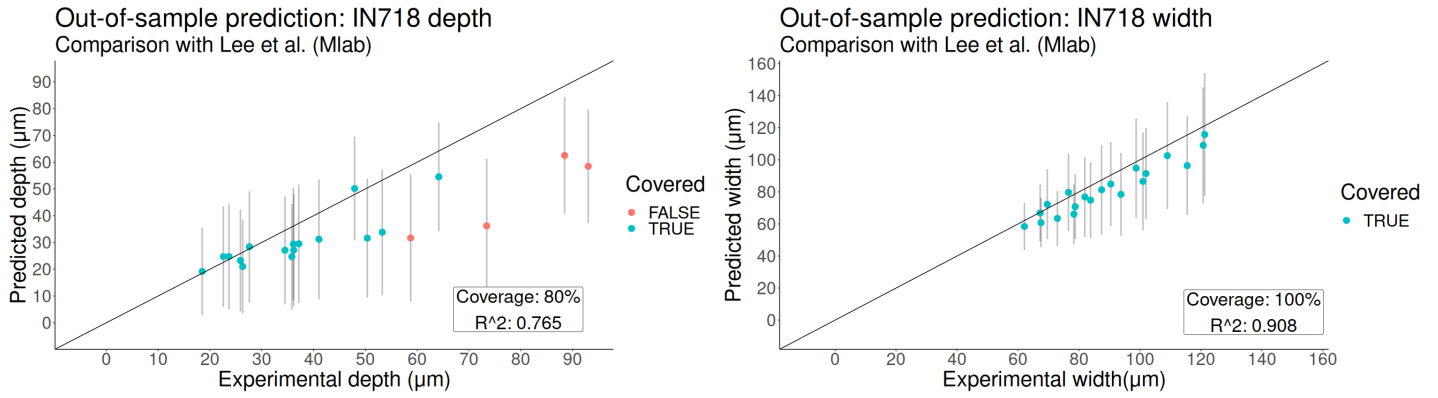


Figure S-23: Predicted melt pool geometry vs. experimental melt pool geometry from Lee et al. [8], Mlab machine data. After calibration, the modified ET model is able to generalize reasonably well to experiments with similar processing conditions.

S8 Printmaps

This section contains printmaps for Ti6Al4V and SS316L, which faced data challenges in computation. Both datasets were more varied and heterogenous than the Lee et al. [8] data for IN625 and IN718. The data from Vaglio et al. [12] used a measurement technique inconsistent with our methodology, e.g reporting the track width rather than the melt pool width. For SS316L, only small beam diameters were present in the data (around 62-50 μm) making the applicability of the model to moderate beam diameters (e.g around 100 μm) difficult.

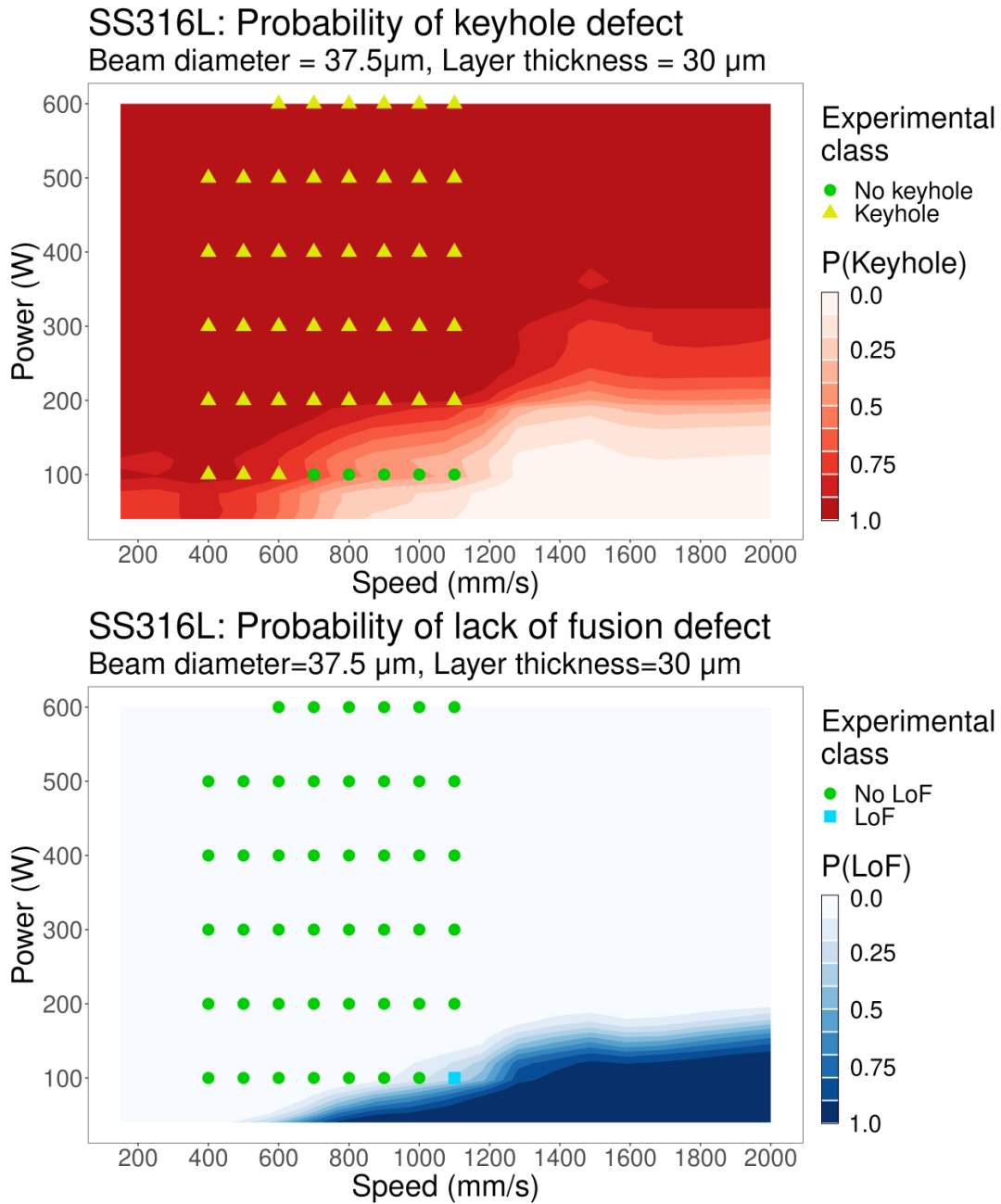


Figure S-24: Probabilistic printability maps for SS316L. The top figure shows the probability of keyhole predictions, and the bottom figure shows the probability of lack of fusion predictions, both computed for a beam diameter of $37.5\mu\text{m}$ and a layer thickness of $30\mu\text{m}$. The data from Goossens et al. [3]. keyhole region may be very large due to the small beam diameters present in the data set. This made predictions for moderate beam diameters (about $100\mu\text{m}$) difficult, as the parameters obtained for the calibration data set were only applicable to these smaller diameters. See Section 3.3 of the main paper for more information.

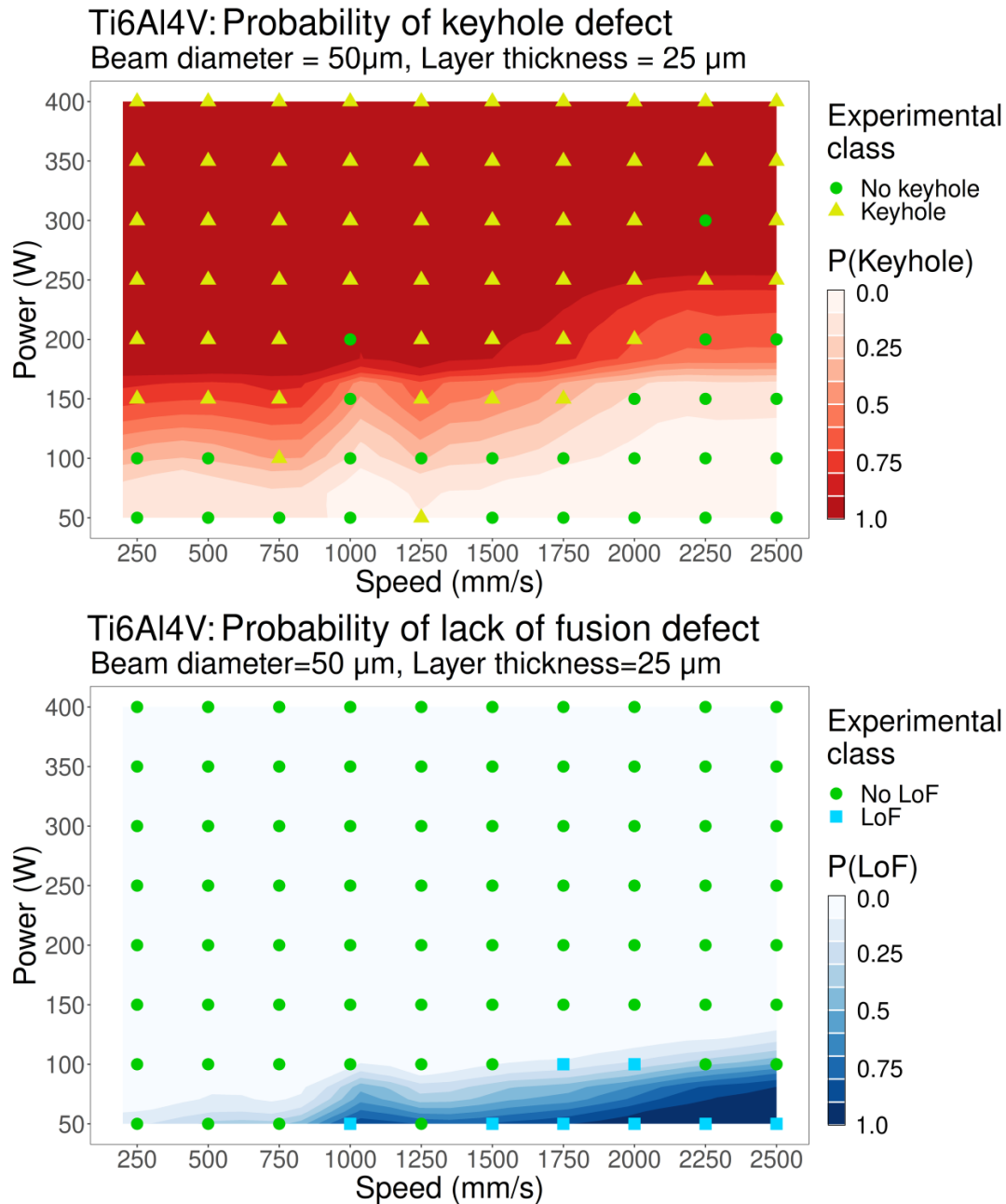


Figure S-25: Probabilistic printability maps for Ti6Al4V. The top figure shows the probability of keyhole predictions, and the bottom figure shows the probability of lack of fusion predictions. The keyhole region appears to be over-predicted due to the measurement technique used by Vaglio et al. [12] of treating the track width as the width, rather than the melt-pool width. The track width is smaller than the melt pool width. This means that the width in the criterion $w/d < 1.5$ used by Johnson et al. [5] is smaller than expected, artificially decreasing the w/d ratio and increasing the probability of keyholing. Nonetheless, it can be seen that the model successfully captures the boundaries present in the data.

References

- [1] J J S Dilip, Ashabul Anam, and Deepankar Pal Brent Stucker. “A Short Study on the Fabrication of Single Track Deposits in SLM and Characterization”. en. In: (2016), p. 16.
- [2] J. J. S. Dilip et al. “Influence of processing parameters on the evolution of melt pool, porosity, and microstructures in Ti-6Al-4V alloy parts fabricated by selective laser melting”. en. In: *Progress in Additive Manufacturing* 2.3 (Sept. 2017), pp. 157–167. ISSN: 2363-9520. DOI: 10.1007/s40964-017-0030-2. URL: <https://doi.org/10.1007/s40964-017-0030-2> (visited on 10/10/2022).
- [3] Louca R. Goossens and Brecht Van Hooreweder. “A virtual sensing approach for monitoring melt-pool dimensions using high speed coaxial imaging during laser powder bed fusion of metals”. en. In: *Additive Manufacturing* 40 (Apr.

- 2021), p. 101923. ISSN: 2214-8604. DOI: 10.1016/j.addma.2021.101923. URL: <https://www.sciencedirect.com/science/article/pii/S2214860421000889> (visited on 10/10/2022).
- [4] Zhiheng Hu et al. “Formation of SS316L Single Tracks in Micro Selective Laser Melting: Surface, Geometry, and Defects”. en. In: *Advances in Materials Science and Engineering* 2019 (Jan. 2019). Publisher: Hindawi, e9451406. ISSN: 1687-8434. DOI: 10.1155/2019/9451406. URL: <https://www.hindawi.com/journals/amse/2019/9451406/> (visited on 10/10/2022).
- [5] Luke Johnson et al. “Assessing printability maps in additive manufacturing of metal alloys”. en. In: *Acta Materialia* 176 (Sept. 2019), pp. 199–210. ISSN: 1359-6454. DOI: 10.1016/j.actamat.2019.07.005. URL: <https://www.sciencedirect.com/science/article/pii/S1359645419304355> (visited on 10/14/2022).
- [6] Chandrakanth Kusuma. “The Effect of Laser Power and Scan Speed on Melt Pool Characteristics of Pure Titanium and Ti-6Al-4V Alloy for Selective Laser Melting”. MA thesis. Wright State University, 2016. URL: https://corescholar.libraries.wright.edu/etd_all/1510/.
- [7] Brandon Lane et al. “Transient Laser Energy Absorption, Co-axial Melt Pool Monitoring, and Relationship to Melt Pool Morphology”. en. In: *Additive Manufacturing* 36 (Dec. 2020), p. 101504. ISSN: 2214-8604. DOI: 10.1016/j.addma.2020.101504. URL: <https://www.sciencedirect.com/science/article/pii/S2214860420308769> (visited on 10/10/2022).
- [8] Seulbi Lee et al. “Data analytics approach for melt-pool geometries in metal additive manufacturing”. In: *Science and Technology of Advanced Materials* 20.1 (Dec. 2019). Publisher: Taylor & Francis. eprint: <https://doi.org/10.1080/14686996.2019.1671140>. pp. 972–978. ISSN: 1468-6996. DOI: 10.1080/14686996.2019.1671140. URL: <https://doi.org/10.1080/14686996.2019.1671140> (visited on 10/20/2022).
- [9] Binqi Liu, Gang Fang, and Liping Lei. “An analytical model for rapid predicting molten pool geometry of selective laser melting (SLM)”. en. In: *Applied Mathematical Modelling* 92 (Apr. 2021), pp. 505–524. ISSN: 0307904X. DOI: 10.1016/j.apm.2020.11.027. URL: <https://linkinghub.elsevier.com/retrieve/pii/S0307904X2030679X> (visited on 02/02/2023).
- [10] Sagar Patel and Mihaela Vlasea. “Melting modes in laser powder bed fusion”. en. In: *Materialia* 9 (Mar. 2020), p. 100591. ISSN: 2589-1529. DOI: 10.1016/j.mtla.2020.100591. URL: <https://www.sciencedirect.com/science/article/pii/S2589152920300089> (visited on 10/20/2022).
- [11] Umberto Scipioni Bertoli et al. “On the limitations of Volumetric Energy Density as a design parameter for Selective Laser Melting”. en. In: *Materials & Design* 113 (Jan. 2017), pp. 331–340. ISSN: 0264-1275. DOI: 10.1016/j.matdes.2016.10.037. URL: <https://www.sciencedirect.com/science/article/pii/S0264127516313363> (visited on 10/20/2022).
- [12] Emanuele Vaglio et al. “Single tracks data obtained by selective laser melting of Ti6Al4V with a small laser spot diameter”. en. In: *Data in Brief* 33 (Dec. 2020), p. 106443. ISSN: 2352-3409. DOI: 10.1016/j.dib.2020.106443. URL: <https://www.sciencedirect.com/science/article/pii/S2352340920313251> (visited on 10/10/2022).